Review

Research progress of amorphous catalysts in the field of electrocatalysis

Zhenyang Yu[1], Qi Sun[1], Lianwang Zhang[1], Huan Yang[2], Yuefang Chen[2,4], Junpeng Guo[2], Mengmeng Zhang[2], Zhijia Zhang[2,3,4] (iD), Yong Jiang[2,3]

[1]School of Mechanical Engineering, Tiangong University, Tianjin 300387, China.
[2]School of Material Science and Engineering, State Key Laboratory of Separation Membrane and Membrane Processes, Tiangong University, Tianjin 300387, China.
[3]School of Electronic and Information Engineering, Institute of Quantum Materials and Devices, Tiangong University, Tianjin 300387, China.
[4]Jiangsu Fuyuan Mustard Seed Space New Material Research Institute Co., LTD, Xuzhou 221100, Jiangsu, China.

Correspondence to: Dr. Mengmeng Zhang, School of Material Science and Engineering, State Key Laboratory of Separation Membrane and Membrane Processes, Tiangong University, No. 399 Binshui West Road, Xiqing District, Tianjin 300387, China. E-mail: zhangmm912@tiangong.edu.cn; Dr. Zhijia Zhang, School of Material Science and Engineering, State Key Laboratory of Separation Membrane and Membrane Processes, Tiangong University, No. 399 Binshui West Road, Xiqing District, Tianjin 300387, China. E-mail: zhangzhijia@tiangong.edu.cn

Abstract

Amorphous materials feature unique structures and physicochemical properties, resulting in their synthesis and applications becoming a dynamic and fascinating new research direction. The high specific surface area, abundant active sites, and good electron transport properties endow amorphous materials with excellent electrocatalytic properties, thus appealing to increasing attention. Based on this, the summary of the current research status of amorphous catalysts in the field of electrocatalysis is urgent and important. In this review, the research progress of amorphous catalysts in electrocatalysis is systematically introduced, focusing on the classification, synthesis methods, modification strategies, characterizations, and electrocatalytic application (including hydrogen evolution reaction, oxygen evolution reaction, oxygen reduction reaction, carbon dioxide reduction reaction, and nitrogen reduction reaction). Finally, this review proposes the prospects and challenges for the future development of high-active and high-selectivity amorphous electrocatalysts.

**Keywords:** Amorphous catalysts, modulation strategy, electrocatalysis

INTRODUCTION

To realize the goals of carbon neutrality and carbon peaking, effectively improving the complex international situation, stabilizing the fossil fuel transportation conditions, and decreasing traditional energy use are at the heart of the matter[1-9]. A feasible strategy is to develop clean and sustainable energy systems via electrocatalysis that can both produce and store energy[10-15]. Compared to traditional energy conversion and storage, electrocatalysis features the merits of high efficiency[16], low carbon emissions[17], and controllability. Importantly, electrocatalysis can utilize intermittent solar and wind energy to drive sustainable energy conversion and storage[18-20], extremely mitigating energy and ecological crises. The sustainable energy from different electrocatalysis processes relies on various reaction mechanisms[21-23], while their realization and ultimate commercialization must depend on the development of high-performance electrocatalysts. The design of highly active stability electrocatalysts needs to consider the following three factors: (1) Intrinsic activity[24]; (2) electron transfer capacity[25]; and (3) diffusion ability of the substance. As the widely recognized high-quality electrocatalysts, the large-scale applications of noble metals (Pt, Au, Ru, Ir, *etc.*)-based materials are severely limited by low reserve and high price[26,27]. Thus, designing high-active and low-cost innovative electrocatalysts is crucial for the development of sustainable energy and ecological systems.

Recently, amorphous catalysts have exhibited unique structural and chemical properties, becoming promising electrocatalytic candidates and receiving a growing interest and potential in oxygen evolution reaction (OER), hydrogen evolution reaction (HER), oxygen reduction reaction (ORR), carbon dioxide reduction reaction (CO_2RR), nitrogen reduction reaction (NRR), and so on[28-32]. The tunability in composition, morphology, active sites, and surface properties provides an attractive platform to improve catalytic activity, stability, and selectivity. As illustrated in Figure 1A, the factors in amorphous catalysts that facilitate electrocatalytic performances are superior to those of crystalline catalysts. In detail, amorphous materials feature short-range order but long-range disorder, resulting in high-density defects and high surface area[33]. The increased surface area endows amorphous catalysts with more active sites for catalytic reactions and exhibits enhanced catalytic activity. Secondly, the tunable composition makes it easy to incorporate heteroatoms in amorphous catalysts, thus significantly enhancing catalytic properties[34]. Thirdly, the disordered atomic structure of amorphous catalysts promotes efficient charge transfer[35], reactant diffusion, and adsorption-desorption in reaction processes, thus improving catalytic activity. Meanwhile, the presence of defects and dislocations in the amorphous structure can act as active sites, leading to enhanced intrinsic activity of catalysts[36,37]. Fourthly, the absence of grain boundaries and lattice defects restrains amorphous structural degradation and corrosion, delivering long operation stability and catalytic activity at harsh reaction conditions with almost no attenuation[38]. Fifthly, the synthesized methods of amorphous catalysts show diversity, such as sol-gel techniques[39], chemical vapor deposition[40], electrodeposition, *etc.*[41]. These strategies enable amorphous catalysts to tune specific surface morphology, composition, and porosity, which can then be applied to a variety of electrocatalytic reactions. Lastly, compared to crystalline catalysts, the less expensive and abundant precursors endow amorphous catalysts with low cost. The advantages result in the large-scale industrial applications of amorphous catalysts, making them economically viable and becoming a kind of sustainable candidate electrocatalysts.

Per the above analysis, amorphous catalysts exhibit huge application potential in electrocatalysis. In this review, we provide a systematic overview of the recent advances in amorphous catalysts in HER, OER, ORR, CO_2RR, and NRR [Figure 1B]. We first introduced the classification of amorphous catalysts and secondly outlined general preparation methods for amorphous catalysts. Next, we summarized the experimental and theoretical characterizations of amorphous catalysts. We then elaborate on the modification strategies of amorphous catalysts, such as structural design, composition tuning, surface modification, interface
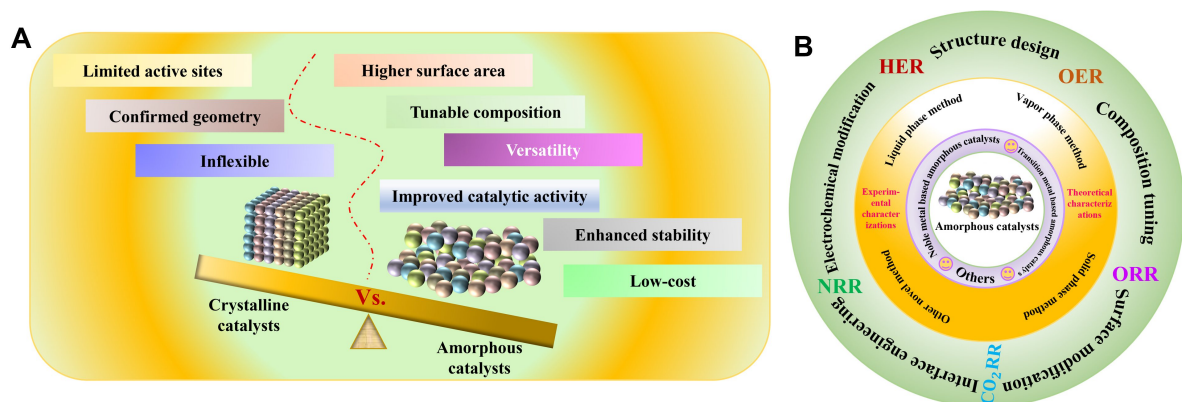
Figure 1. (A) The main characteristic comparison of amorphous and crystalline catalysts. (B) Overview of amorphous catalysts in electrocatalysis.

engineering, *etc*. Moreover, we introduce the applications of amorphous catalysts in various electrocatalytic reactions. Finally, the current challenges and prospects of amorphous catalysts are discussed. We hope this review sheds light on the design of high-active amorphous electrocatalysts and stimulates their extensive applications.

CLASSIFICATION OF AMORPHOUS CATALYSTS

In catalytic reactions, crystalline electrocatalysts are commonly used. This is a class of highly crystalline catalytic materials with a regular lattice structure and well-defined crystal surface orientation, which usually exhibit high catalytic activity and selectivity and have good catalytic effects for some catalytic reactions. Their lattice structure and crystal plane orientation can provide good surface active sites, which is favorable for the catalytic reactions[42]. Common crystalline catalysts include spinel-type, chalcogenide-type, *etc*. An effective bifunctional catalyst for overall water splitting was established using a mesoporous NiFe-oxide nanocube (NiFe-NC) system based on NiFe Prussian blue analog metal-organic frameworks (MOFs)[43]. When water splitting was tested in an alkaline solution, the overpotentials of NiFe-NCs for HER and OER reached 197 and 271 mV, respectively, at a current density of 10 mAcm^{-2}, indicating good catalytic performance. A novel lanthanide-based high-entropy chalcogenide (HEPO) electrocatalyst for oxygen precipitation reaction was reported by Nguyen *et al.*[44]. The optimized La(CrMnFeCo$_2$Ni)O$_3$ HEPO had an OER overpotential of 325 mV at a current density of 10 mA cm^{-2} and had excellent electrochemical stability after testing for 50 h. Single-phase nanoporous high-entropy alloy (HEA) np-AlNiCoFeX (X = Mo, Nb, Cr) catalysts with high-entropy (oxygen) hydroxide (HEO) overlayers prepared by combining precursor alloy design with chemical etching exhibited excellent OER activity by Qiu *et al.*[45]. AB$_2$O$_4$ (A = Zn^{2+}; B = Mn^{3+}/Co^{3+}) catalysts with hollow porous spinel structures exhibited excellent oxygen reduction activity in fuel cells and metal-air batteries[46]. Among them, the ZnMnCoO$_4$ microspheres showed the best ORR activity with a half-wave potential only 50 mV lower than that of Pt/C and excellent durability in alkaline solutions (after 10,000 s, it retained more than 95% of the initial current). Fang *et al*. prepared three NiCo$_2$O$_4$ nanocrystals exposed to different crystal planes[47]. The results showed that NiCo$_2$O$_4$ nanosheets (NSs) exposed (110) crystal planes exhibited the best OER catalytic activity.

However, with the continuous improvement of performance requirements for catalytic materials, people have discovered that there are certain limitations in achieving ideal catalytic effects solely by relying on crystal structure and crystal plane orientation[48] because, in catalytic reactions, the configuration of surface active sites, the surface defect structure of the catalyst, grain boundaries and intragranular defects may all

affect the catalytic performance. To overcome these limitations, amorphous catalysts have become the focus of attention. Amorphous catalysts are catalytic materials with amorphous or amorphous structures, which are rich in defect structures, pore structures, and higher surface activity. This structural flexibility and tunability allows amorphous catalysts to be better adapted to different catalytic reactions and provide more active sites. For example, Altaf *et al*. first synthesized $LaCoO_3$ with a chalcogenide structure, followed by an amorphization process via urea reduction and tailored modifications[49]. The results showed that the amorphous $LaCoO_3$ (abbreviated as LCO-4) has a high electrochemical active area and exhibited excellent OER activity and stability superior to that of pristine $LaCoO_3$, confirming that its unique disordered structure is one of the key factors in improving the catalytic performance.

In the history of amorphous structures in electrocatalysis, amorphous catalysts can be roughly divided into noble metal-based and transition metal-based amorphous catalysts. Taking cost and industrialization into consideration, recent research for amorphous catalysts is mostly focused on transition metal-based materials rather than noble metal-based materials.

Noble metal-based amorphous catalysts
Precious metal-based catalysts (such as Pt-based, Ir-based, Ru-based, *etc*.) are widely used as electrocatalysts; however, their high cost limits their large-scale applications. Optimizing their inherent activity, increasing active sites, and improving operational stability are urgent. Amorphization endows noble metal-based amorphous catalysts with unique surface and active site distribution, improving reaction efficiency and selectivity, thus receiving increasing attention in electrocatalysis. For example, excellent acidic OER performances were measured in amorphous IrO_x (a-IrO_x) thin film catalysts rather than crystalline IrO_x thin films[50], whose overpotentials at 1 and 10 mA cm^{-2} were 190 and 220 mV, respectively. Moreover, Pd_2RuO_x materials[51] were synthesized by confining atomically thin Pd-PdO nanodomains in amorphous metallic ruthenium oxide (RuO_2) NSs and then performing a reduction treatment [Figure 2A], which exhibited excellent electrocatalytic activity in electrolyzing water. The presence of Pd-PdO heterogeneous interfaces and numerous surface defects in materials facilitates active substance adsorption and thus promotes the electrocatalytic reaction [Figure 2B]. Na-modified defect-rich crystalline/amorphous rutile structure RuO_2 (a/c-RuO_2) catalysts delivered excellent OER catalytic stability [Figure 2C], benefiting from the abundant defects, grain boundaries, and accessibility of active sites[52].

Given the small reserves and expensive nature of precious metals, reducing their active loading without affecting the overall electrocatalytic efficiency is one of the cost-effective strategies. The Pt-a/c-NiCoHPi catalyst with crystalline/amorphous structure (Pt content is only 2.1%) exhibited excellent HER activity in alkaline solution, with an overpotential of only 19 mV at 10 mA cm^{-2} [Figure 2D][53]. Wang *et al*. synthesized amorphous PdCu nanorods with controllable size and morphology [Figure 2E] and used them for ethanol electrooxidation reaction[54]. The prepared amorphous PdCu nanorods delivered a high Faraday efficiency (FE) of 69.6% for C1 products, which was much higher than that of the corresponding crystalline catalysts and the commercial Pd/C [Figure 2F]. Density-functional-theory (DFT) calculations further revealed that the amorphous structure can significantly reduce the energy barrier for C-C bond breaking on the surface of the PdCu catalysts and promote the kinetic process of the ethanol oxidation reaction [Figure 2G]. Despite the remarkable progress of noble metal-based amorphous catalysts in the field of electrocatalysis, there are still challenges and issues, such as the high cost and stability of noble metal catalysts. Therefore, the development of amorphous catalyst materials with economic benefits and high reactivity is one of the hot spots for future research.
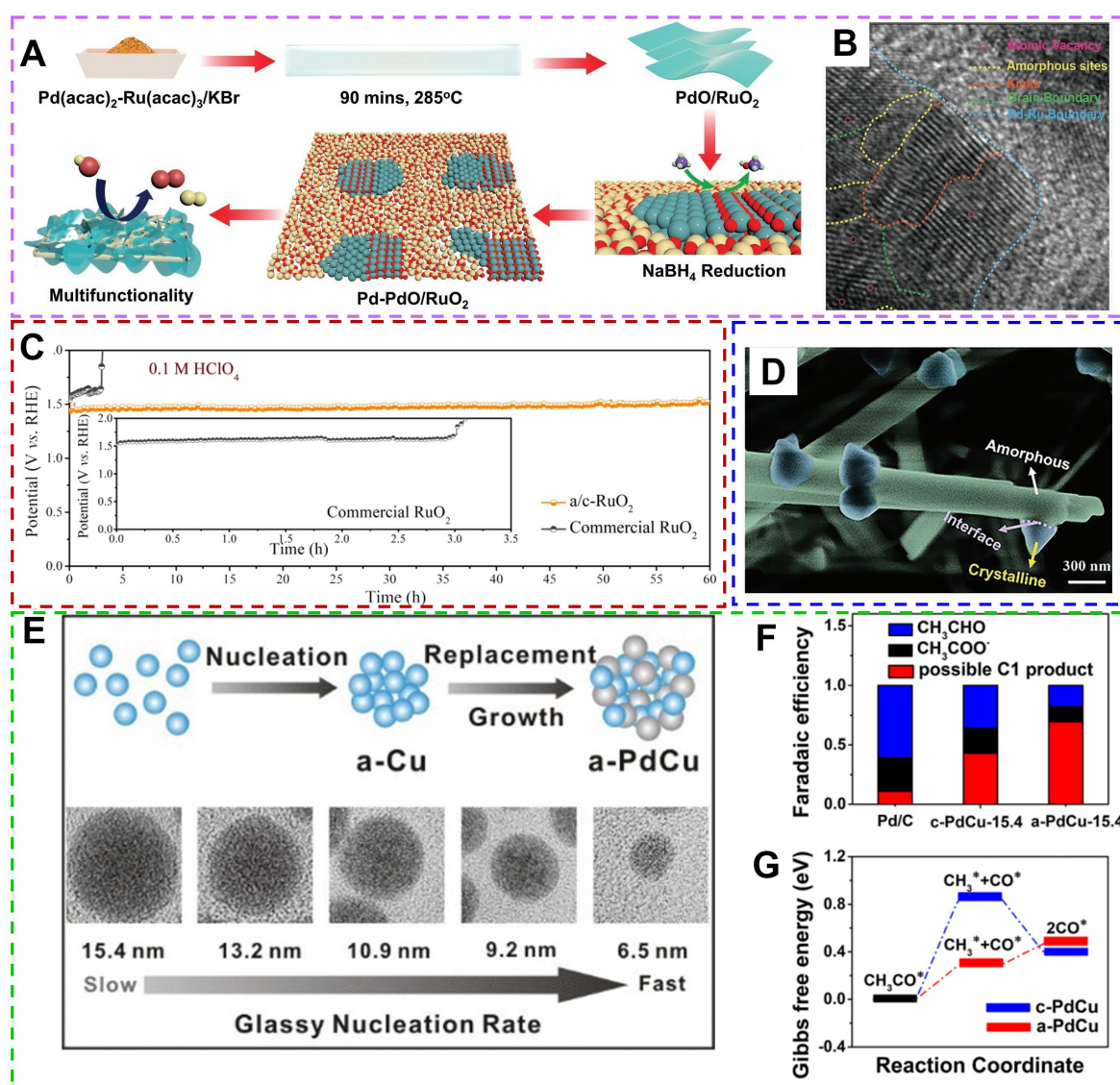
Figure 2. (A) The synthesis of PdRuO$_x$ materials; (B) HRTEM image of Pd$_2$RuO$_x$-0.5 h. (Reproduced with permission[51]. Copyright 2023, WILEY-VCH). (C) Chronopotentiometry measurement results for a/c-RuO$_2$ and commercial RuO$_2$ at 10 mA cm^{-2} in 0.1 M HClO$_4$. (Reproduced with permission[52]. Copyright 2021, WILEY-VCH). (D) High-magnification SEM images of Pt-a/c-NiCoHPi. (Reproduced with permission[53]. Copyright 2023, WILEY-VCH). (E) Schematic illustration of the size-controllable synthesis of a-PdCu nanoparticles. (F) FE of different products; (G) Gibbs free energy diagram of the EOR on a-PdCu and c-PdCu model catalysts in the C1 path. (Reproduced with permission[54]. Copyright 2022, American Chemical Society).

Transition metal-based amorphous catalysts

Thanks to the abundant earth reserves and cost-effectiveness, amorphous catalysts composed of non-noble transition metal elements have been widely studied in electrocatalysis. For instance, Jiang *et al.*[55] prepared self-supported FeNiCo-based amorphous catalysts with hierarchical micro/nanopore structures by dealloying amorphous/nanocrystalline precursors [Figure 3A]. The optimized electrocatalyst showed a HER overpotential of 134 mV and an OER overpotential of 206 mV at 10 mA cm^{-2} in alkaline solution. The main reason is that amorphous nanoporous frameworks can provide fast reaction kinetics, abundant active sites, and enhanced electrochemically active surface area. The synergistic effect of the structural and compositional advantages of the catalysts finally showed excellent catalytic activity.
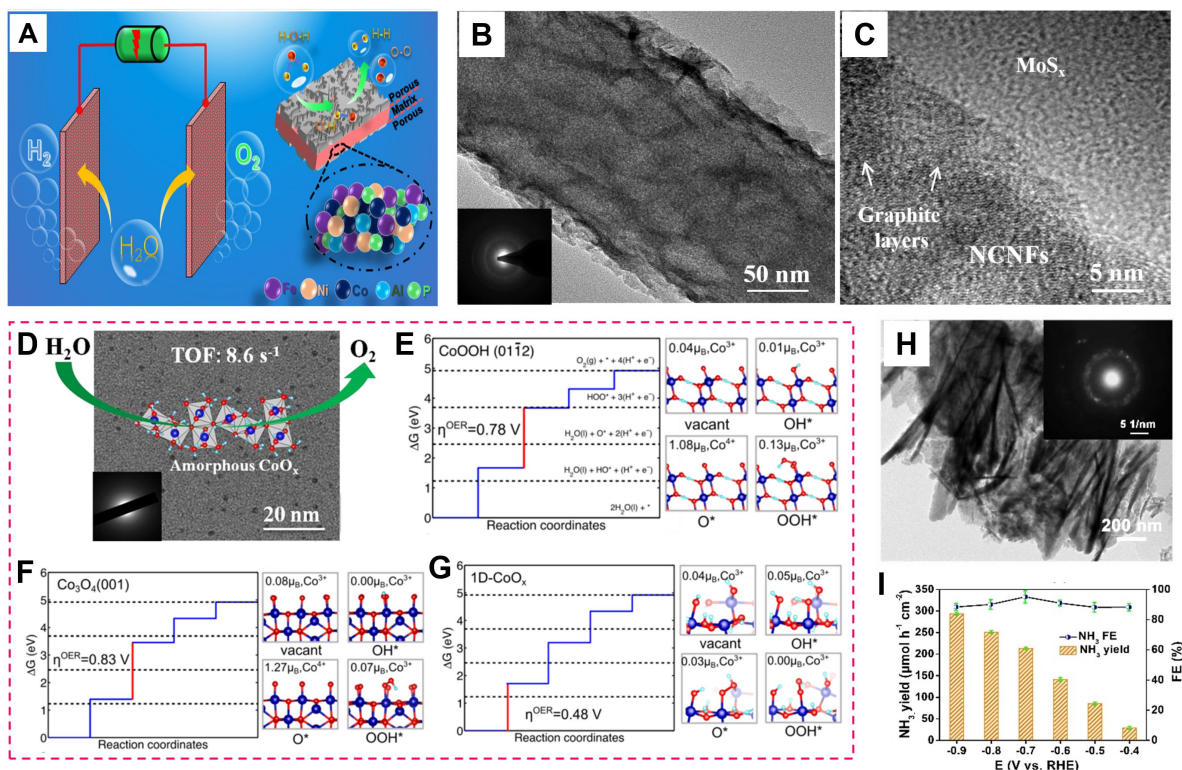
Figure 3. (A) Schematic diagram of self-supported hierarchical porous amorphous FeNiCo-based bifunctional catalysts. (Reproduced with permission[55].Copyright 2021, Elsevier). (B) TEM and (C) HRTEM image of MoS$_x$@NCNFs-30 films. (Reproduced with permission[56].Copyright 2016, Elsevier). (D) HRTEM diagram of amorphous CoO$_x$ nanoparticles (The insert shows its SAED patterns); (E-G) Free energy diagram for the water oxidation on Co$_3$O$_4$,CoOOH, and 1D-CoO$_x$ surfaces. (Reproduced with permission[57]. Copyright 2017, WILEY-VCH). (H) TEM image and SAED pattern (inset) of CoB@TiO$_2$ nanosheets; (I) NH$_3$ yields and FE at given potentials. (Reproduced with permission[59].Copyright 2022, CCS).

Novel amorphous flower-like molybdenum sulfide@nitrogen doped carbon nanofiber (MoS$_x$@NCNFs) thin films were synthesized and used to reduce water[56]. MoS$_x$ NSs immobilized on NCNFs in a unique flower-like structure were detected in the transmission electron microscope (TEM) image [Figure 3B], while the amorphous structure of MoS$_x$ was confirmed by selected area electron diffraction (SAED) (inset of Figure 3B) and Figure 3C. The MoS$_x$@NCNFs exhibited excellent HER catalytic activity, with an overpotential of 137 mV at 10 mA cm^{-2}. Amorphous cobalt oxide nanoparticles (ca. 2 nm) acted as water oxidation catalysts with a turnover frequency of up to 8.6 s^{-1} in the Ru(bpy)$_3$$^{2+}$-Na$_2S_2O_8$ system [Figure 3D], which is superior to that of the most active homogeneous cobalt-based molecules[57]. Meanwhile, theoretical calculations showed that the obtained structure promotes O-O bond coupling and improves the water oxidation activity compared with crystalline cobalt oxide [Figure 3E-G], further confirming the good activity of amorphous cobalt oxide nanoparticles. Pang *et al.* used a simple electrochemical dealloying method to prepare a self-supporting amorphous NiFeCoP catalyst with a nanoporous structure (np-NiFeCoP)[58]. The np-NiFeCoP catalyst exhibited good electrocatalytic activity from its unique structural characteristics, which can expose more active sites and exert synergistic effects between metal elements. In 1.0 M KOH alkaline solution, the overpotentials of HER and OER were 105 and 244 mV for np-NiFeCoP catalyst at 10 mA cm^{-2}, respectively. Amorphous transition metal boride (TMB) nanomaterials featured numerous defects and dangling bonds, thus providing abundant active sites for the electrocatalytic nitrite reduction reaction (NO$_2$$^-$RR). CoB@TiO$_2$/Ti plate (TP) was prepared by sputtering an amorphous cobalt boride nanofilm on the surface using titanium dioxide (TiO$_2$) NS arrays as a substrate by Hu *et al.*

[Figure 3H][59]. The prepared CoB@TiO$_2$/TP showed a high NH$_3$ yield of up to 233.1 μmol h^{-1} cm^{-2} at -0.7 V and a FE of 95.2% for NO$_2^-$RR, superior to most reported NO$_2^-$RR catalysts [Figure 3I].

As one kind of emerging catalyst, transition metal-based amorphous catalysts present many unique properties and application potential. However, its industrialization and commercial applications still face several challenges, such as production cost, catalyst stability, and scale-up preparation. Therefore, future development requires further strengthening of the industrialization technology research and economic feasibility analysis.

Other types of amorphous catalysts

Recently, HEAs and high-entropy oxides (HEOs) composed of five or more elements have become a research hotspot in the field of catalysts due to their tunable electronic structure and wide range of component selection[60]. Among them, the design of multi-component high-entropy catalysts helps to improve the catalytic activity and stability of the catalysts. In addition, amorphous high-entropy catalysts have disordered local structures, which can provide more reaction active sites and exhibit superior catalytic performance. For example, Wang *et al.* prepared nanostructured amorphous Fe$_{29}$Co$_{27}$Ni$_{23}$Si$_9$B$_{12}$ HEA strips and used them as electrocatalysts for OER [Figure 4A][61]. Thanks to their highly disordered configuration, they exhibited excellent catalytic activity in electrocatalytic activity tests, with an overpotential of only 230 mV at a current density of 10 mA cm^{-2} [Figure 4B]. The amorphous FeCoNiPB HEOs prepared by a chemical reduction strategy were reported by Wang *et al.*[62]. When OER testing was performed in alkaline media, its catalytic performance was superior to quaternary metal oxides such as FeCoPB and the commercial catalyst RuO$_2$. This can be attributed to its unique amorphous structure and the synergistic effect of multiple components, making it capable of exerting excellent catalytic performance. In order to activate the surface atoms of HEOs, Li *et al.* constructed low-crystallinity (Fe, Co, Ni, Mn, Zn)$_3$O$_4$ (HEO-Origin) NSs with abundant oxygen vacancies [Figure 4C], whose TEM images and the corresponding SAED images showed their amorphous nature [Figure 4D and E][63]. Due to its large specific surface area, high activity of surface atoms and the presence of oxygen vacancies, HEO-Origin exhibits excellent OER activity.

Rare earth elements have more unpaired electrons and irregular electron arrangement, which makes rare earth catalysts have high catalytic activity. Rare earth amorphous catalysts are an attractive class of catalysts with abundant active sites and defects in their structures, which provide more reaction sites and further enhance their catalytic activity. Yan *et al.* reported rare earth metal oxide electrocatalysts composed of ultrathin amorphous La$_2$O$_3$ NSs hybridized with uniform La$_2$O$_3$ nanoparticles [Figure 4F][64]. As shown in Figure 4G, the SAED pattern of the NS surfaces showed broad and diffuse diffraction rings, indicating that La$_2$O$_3$@ NP-NS indeed has a large number of amorphous phases with small crystals. Among them, the La$_2$O$_3$@NP-NS catalyst with a NS thickness of 2.27 nm exhibited excellent OER activity with an overpotential of 310 mV at 10 mA cm^{-2}. This can be attributed to the ultra-thin thickness, which shortens the charge diffusion path and promotes electron transfer and enhanced reaction kinetics. For the amorphous Ni-Nb-Y alloy, the catalytic activity of HER can be optimized by controlling the concentration and distribution of Y in the ternary alloy system[65]. Among them, the Ni$_{81.3}$Nb$_{6.3}$Y$_{12.5}$ catalyst, in which the amorphous phase coexists with a small amount of crystalline phase, exhibits the highest HER activity. Sun *et al.* obtained amorphous Mn-Ce-O$_x$, Mn-La-O$_x$ and Mn-Pr-O$_x$ by doping Mn-based catalysts with rare earth metals (Ce, La or Pr). Among them, the Mn-Ce-O$_x$ catalyst has the best oxidation performance[66]. At a reaction temperature of 239 °C, the maximum oxidation conversion rate of NO is 94.0%. LCO-4 has been proven to have excellent OER activity [Figure 4H and I][49]. At a current density of 50 mA cm^{-2}, the overpotential is only 350 mV, and the extremely low Tafel slope (70 mV dec^{-1}) further highlights its remarkable activity.
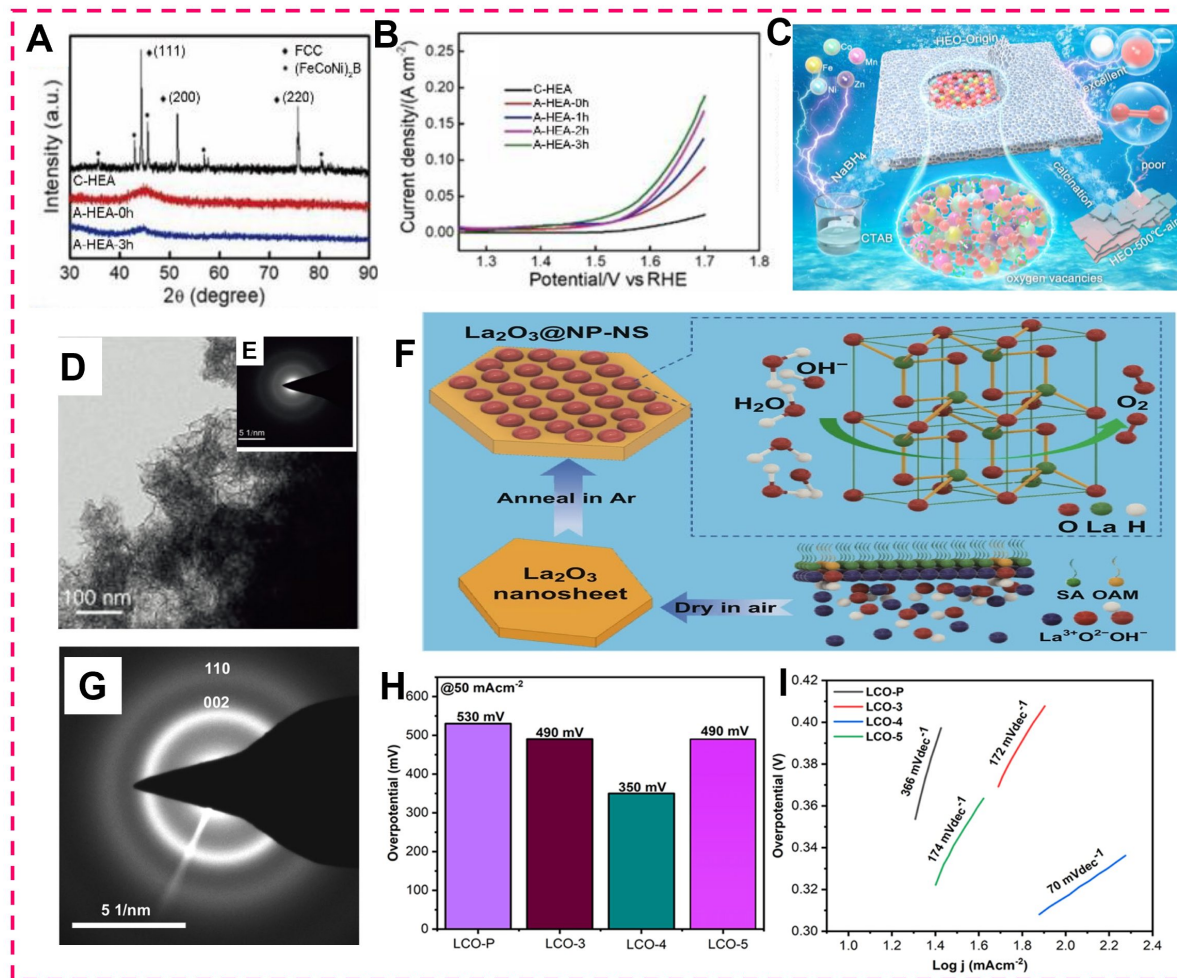
Figure 4. (A) XRD patterns of various samples. (B) LSV polarization curves of different catalyst electrodes for the OER in 1.0 M KOH. (Reproduced with permission[61]. Copyright 2022, Springer). (C) Schematic diagram of HEO-Origin preparation. (D) TEM image and (E) SAED patterns of HEO-Origin. (Reproduced with permission[63]. Copyright 2023, Elsevier). (F) Schematic diagram of the synthesis of La$_2$O$_3$@NP-NS. (G) SAED pattern of La$_2$O$_3$@NP-NS. (Reproduced with permission[64]. Copyright 2020, Springer). (H) Overpotential bar graph and (I) Tafel plot of different catalyst electrodes. (Reproduced with permission[49]. Copyright 2023, Wiley-VCH GmbH).

SYNTHESIS METHOD OF AMORPHOUS CATALYSTS

In the history of amorphous catalyst preparation, numerous synthesized strategies have been developed and can be broadly categorized into liquid, vapor, and solid phases.

Liquid phase method

The liquid phase method dissolves the desired atoms or molecules in a liquid solution and then forms amorphous catalysts; the synthesis process needs to control parameters such as temperature, concentration, pH, *etc.*[67,68]. The atoms or molecules dissolve in the solution and combine to form an amorphous catalyst via chemical reactions or precipitations. This method features the merits of simple operation, easily controlled reaction conditions[69], diverse catalyst morphology, *etc.*, thus receiving extensive attention. The typical liquid phase method contains the sol-gel method, deposition method, hydrothermal method, *etc.*

(1) Sol-gel method: The metal alkoxides or metal salts in a solution undergo hydrolysis and condensation to form a sol, followed by gelation and drying to obtain a solid material. This method has the advant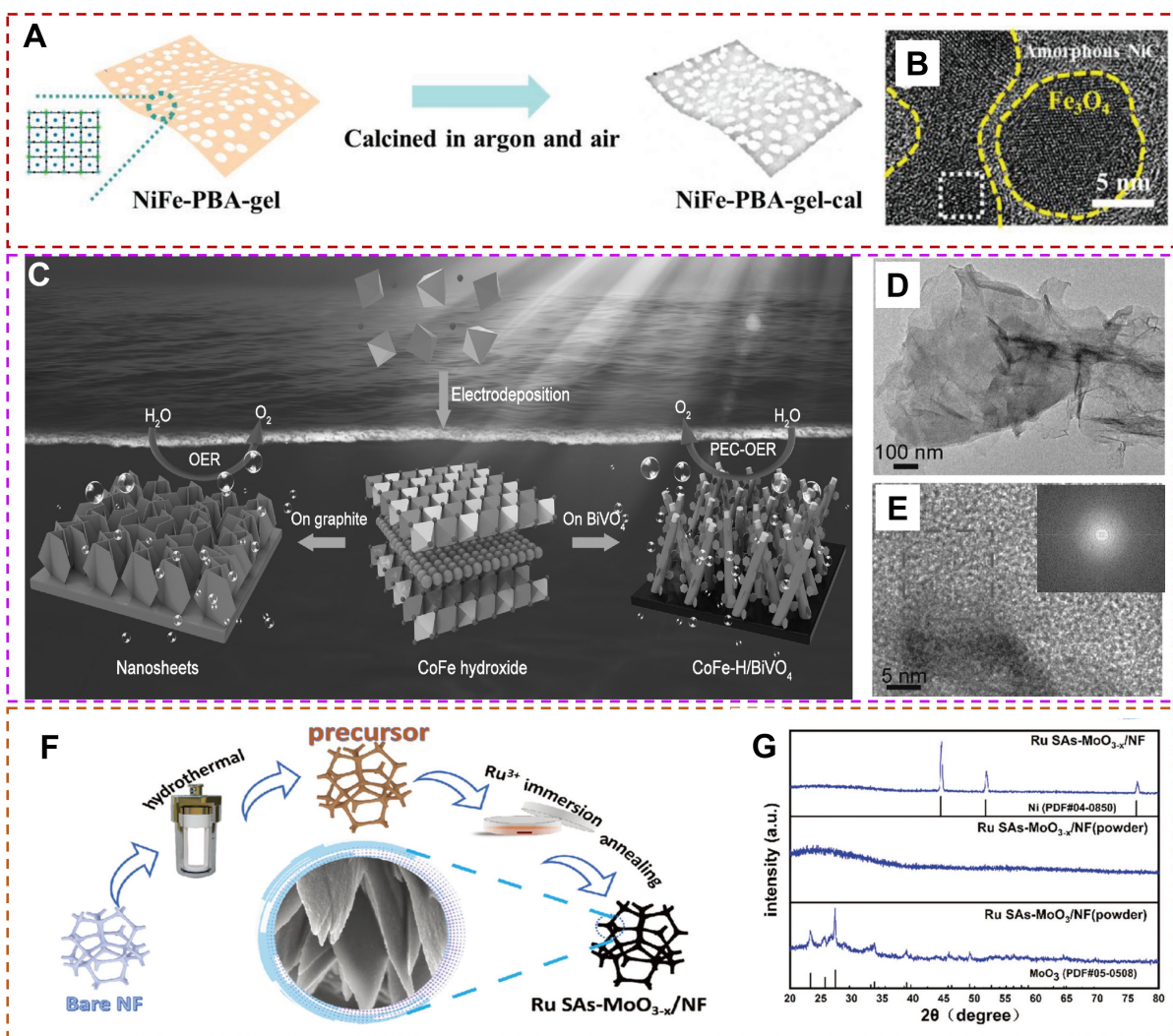ages of low-temperature processing, high degree homogeneity, and excellent controllable catalyst size and morphology. For example, Zhang *et al.* used a sol-gel method to prepare a Prussian blue analog (NiFe-PBA) precursor with a two-dimensional (2D) network and then further annealed it into a Fe_3O_4/NiC_x composite (NiFe-PBA-gel-cal), as a bifunctional electrocatalyst for seawater splitting [Figure 5A][70]. It can be seen from the high-resolution TEM (HRTEM) image of the calcined composite material that NiC_x contains both amorphous and crystalline phases [Figure 5B], which is beneficial to the catalytic activity in electrochemical tests. Furthermore, the amorphous Cr_8Co_1-300 catalyst from the sol-gel method was reported[71], which exhibits a high specific surface area.

(2) Deposition method: Depositing a metal precursor or its compound in a solution on a suitable carrier surface. This method includes the impregnation method, brush coating method, suspension deposition method, *etc.* Generally, amorphous metal alloys, carbon-based amorphous materials, amorphous nanocomposites, *etc.*, can be prepared via the deposition method. For instance, amorphous cobalt iron hydroxide (CoFe-H) NSs were synthesized by electrodepositing CoFe-H NSs on graphite at 1.42 V [Figure 5C][72]. The characterizations of the TEM, HRTEM, and fast Fourier transform (FFT) reveal the amorphous character of CoFe-H NSs [Figure 5D and E]. Moreover, a novel pulsed electrodeposition method was used to dissolve commercially available anodic aluminum oxide (AAO) nano-molds in an alkaline solution that contained Ni-, Pd-, and P-ions[73]. In the electrodeposition process, amorphous Ni-P and Ni-Pd-P nanowire structures were formed by controlling the pulsed currents and potentials. Furthermore, the electrodeposition method can quickly produce unique three-dimensional (3D) nano-dendrite forests of amorphous α-phase mixed nickel-cobalt hydroxides on stainless steel foil[74].

(3) Hydrothermal method: A direct method to prepare amorphous catalysts with no need for complex machines or working conditions[75,76]. Typically, the precursor only interacts with a solvent (often water) for a brief amount of time at a high temperature and high pressure to synthesize catalysts. The reaction conditions of high temperature and high pressure ensure the complete dispersion and dissolution of the solvent and precursor, benefiting the uniform reaction and the even distributed active sites. On the other hand, combining reaction temperature and time can tune the morphology, pore structure, and surface characteristics of amorphous catalysts, finally modifying catalytic performances. For example, the basic La^{3+} from the prepared bulk-phase $LaNiO_3$ chalcogenide oxides would selectively dissolve in $FeCl_3$ solution [reaction (1)][77]. With the consumption of H^+, in the reaction process, part Fe^{3+} was hydrolyzed and deposited on the surface of the residual substrate [reaction (2)]. Noticeably, the La^{3+} in LaNiFe hydroxide stemmed from the residual substrate rather than the solution. The successive leaching of the large-sized La^{3+} ions induces the crystalline chalcogenide structure to gradually collapse and turn into an amorphous state, thus generating a novel amorphous Ni-Fe-based OER electrocatalyst. Moreover, the precursor grown on the surface of nickel foam (NF) by hydrothermal process was immersed in $RuCl_3$ solution and annealed in air to prepare the amorphous molybdenum-based oxide stabilized single-atomic-site (Ru-SAs-MoO_{3-x}/NF) catalysts [Figure 5F][78]. The X-ray diffraction (XRD) of the scraped powder from the Ru-SAs-MoO_{3-x}/NF surface indicates almost no characteristic peaks [Figure 5G], suggesting its amorphous nature.

$$LaNiO_3 + H^+ \rightarrow \text{edge-shared } [Ni^{3+}O_6] + La^{3+} + H_2O \tag{1}$$

$$La^{3+} + \text{edge-shared } [Ni^{3+}O_6] + Fe^{3+} + OH^- \rightarrow \text{LaNiFe hydroxide} \tag{2}$$
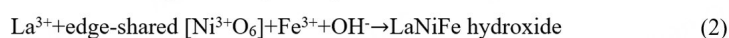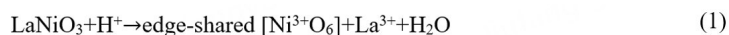
Figure 5. (A) Schematic diagram of the synthesis of NiFe-PBA-gel-cal. (B) HRTEM image of NiFe-PBA-gel-cal. (Reproduced with permission[70]. Copyright 2022, Wiley-VCH). (C) Schematic illustration of CoFe-H structure and its application in electrochemical and photo-electrochemical water oxidation as an OER electrocatalyst. (D) TEM, and (E) HRTEM images of CoFe-H nanosheets (the insert is corresponding FFT). (Reproduced with permission[72]. Copyright 2017, WILEY-VCH). (F) The fabrication illustration of Ru SAs-MoO$_{3-x}$/NF. (G) XRD patterns of Ru SAs-MoO$_{3-x}$/NF and Ru SAs-MoO$_3$/NF. (Reproduced with permission[78]. Copyright 2023, WILEY-VCH).

Vapor phase method

Amorphous catalysts from a vapor phase approach need to combine atoms or molecules in a specific ratio in an inert atmosphere before causing them to react on the catalyst surface. This method presents significant merits in terms of high purity[79], homogeneity[80], controllability, and specific surface area, facilitating the synthesis of amorphous catalysts with complex components. Typically, vapor phase methods can be classified as the physical vapor phase deposition (PVD) and chemical vapor phase (CVD).

Physical Vapor Deposition (PVD): This method refers to depositing thin metal or metal compound films onto a substrate by a physical process, such as sputtering, evaporation, pulsed laser deposition, *etc.*[81,82]. The attractiveness is the precise control of deposition conditions, allowing the formation of an amorphous film with unique structures and excellent catalytic properties. PVD shows outstanding advantages in terms of elaborately regulating the thickness and composition of amorphous films. For instance, a thin conformal

amorphous IrO_x (a-IrO_x) coating was reported by Smith *et al.*, which was produced at room temperature in an ambient atmosphere by the light-induced breakdown of a photoactive $Ir(acac)_3$ precursor placed on a conducting substrate [Figure 6A][50]. In the XRD pattern, there are no diffraction peaks related to the iridium oxide crystal phase, confirming the amorphous nature of a-IrO_x [Figure 6B]. Moreover, an oxygen-rich vacancy amorphous copper oxide nanofilm (m-CuO_x) catalyst was prepared by a vacuum evaporation method[83], and its amorphous was indexed from the XRD spectrum.

(2) Chemical Vapor Deposition (CVD): This method means depositing metal atoms on a substrate surface by breaking down the gas-phase precursor compound in an inert gas atmosphere[84-86]. Generally, this method can be applied to amorphous metal oxides and carbon-based amorphous materials. For example, a variety of amorphous noble metal NSs less than 10 nm thickness was produced from direct annealing, such as amorphous Ir NSs, amorphous IrRu NSs, amorphous IrRhRu NSs, *etc.* [Figure 6C][87]. The annealed medium is a mixture of metal acetylpyruvates and alkali salts. As shown in Figure 6D and E, the amorphous feature of the prepared Ir NSs was confirmed by TEM and aberration-corrected High-Angle Annular Dark Field-Scanning Transmission Electron Microscopy (HAADF-STEM) characterizations.

Solid phase method

This method refers to preparing materials by using solid-state reactions[88]. In the solid-state reactions for forming amorphous catalysts, the spread and assembly of atoms or molecules can be realized by solid-phase diffusion or physically excited diffusion and aggregation. The solid-phase method, known for its advantages of simple preparation, high controllability, and homogeneity, facilitates the synthesis of amorphous catalysts[89]. Importantly, this method exhibits remarkable advantage in the synthesis of substances that have a high melting point or are unstable in solution. However, the solid-phase method faces several challenges of lower specific surface area, strong crystallinity, high influence from impurities, and strict preparation requirements. Conventionally, the solid phase method includes melt quenching, sputtering, and ball milling.

Melt-quenching method: The reactants first melt at high temperatures, followed by rapid quenching to room temperature or lower. The rapid cooling benefits to forming an amorphous structure rather than a long-range order structure[90]. Commonly, this method is conducted to synthesize amorphous metallic alloys by rapidly solidifying the metal-molten mixture. The prepared amorphous alloys own a high degree of compositional flexibility. For instance, amorphous $Al_{80}Pd_{10}Cu_5Ni_5$ strips with a thickness of 30~50 μm and a width of 2~4 mm [Figure 7A] were reported by Yang *et al.*[91]. In detail, an $Al_{80}Pd_{10}Cu_5Ni_5$ master alloy at Ar atmosphere was first prepared via arc melting. Subsequently, the master alloy in a quartz tube was remelted to a boiling state and sprayed onto a copper roll. Finally, the final amorphous nanoporous PdCuNi-S catalyst was formed by a two-step dealloying method. Moreover, amorphous Ni-Fe alloy strips with a thickness of 25 μm and a width of 2 mm were prepared by using the same synthesis method[92]. The amorphous catalysts from a melting-dumping strip technique feature changed structure and play a better role in the relevant electrocatalytic reactions. This method features the merits of high-speed solidification, uniformity, controllability, and high production efficiency technology, thus receiving wide applications.

Sputtering method: This method utilizes energetic particles to bombard the target material surface, resulting in the metal atoms dissociating from the target material and depositing onto the substrate. For example, an amorphous $Ir_{25}Ni_{33}Ta_{42}$ nano-thick metallic glass (MG) film with low Ir content was grown on a Si substrate by using ion beam deposition (IBD) [Figure 7B][93]. The amorphous structure of the deposited $Ir_{25}Ni_{33}Ta_{42}$ MG thin film was revealed by the HRTEM and related SAED characterizations [Figure 7C]. As a HER electrocatalyst, the obtained amorphous film exhibits high activity and stability in 0.5 M H_2SO_4 solution.
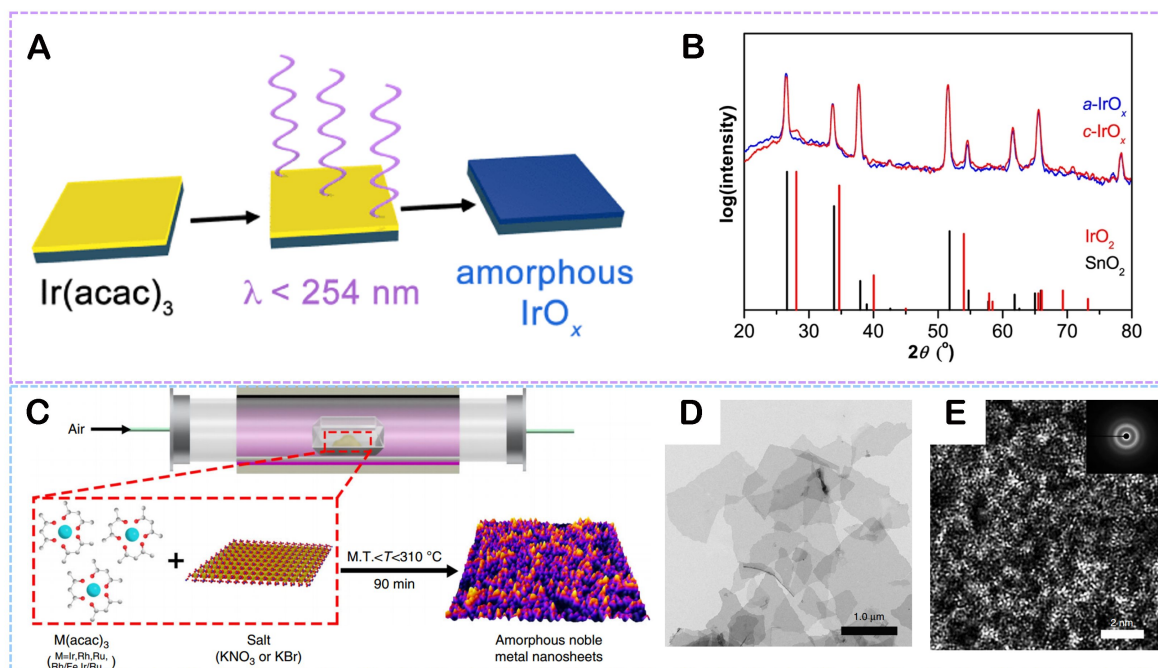
Figure 6. (A) Schematic diagram of the preparation of amorphous IrO_x. (B) X-ray diffraction patterns for a-IrOx and c-IrOx on FTO. (Reproduced with permission[50]. (Copyright 2014, American Chemical Society). (C) The general synthetic process of amorphous noble metal NSs. (D) TEM, and (E) Aberration-corrected HAADF-STEM image of amorphous Ir NSs (the inset in E shows the SAED pattern). (Reproduced with permission[87]. Copyright 2019, Nature).
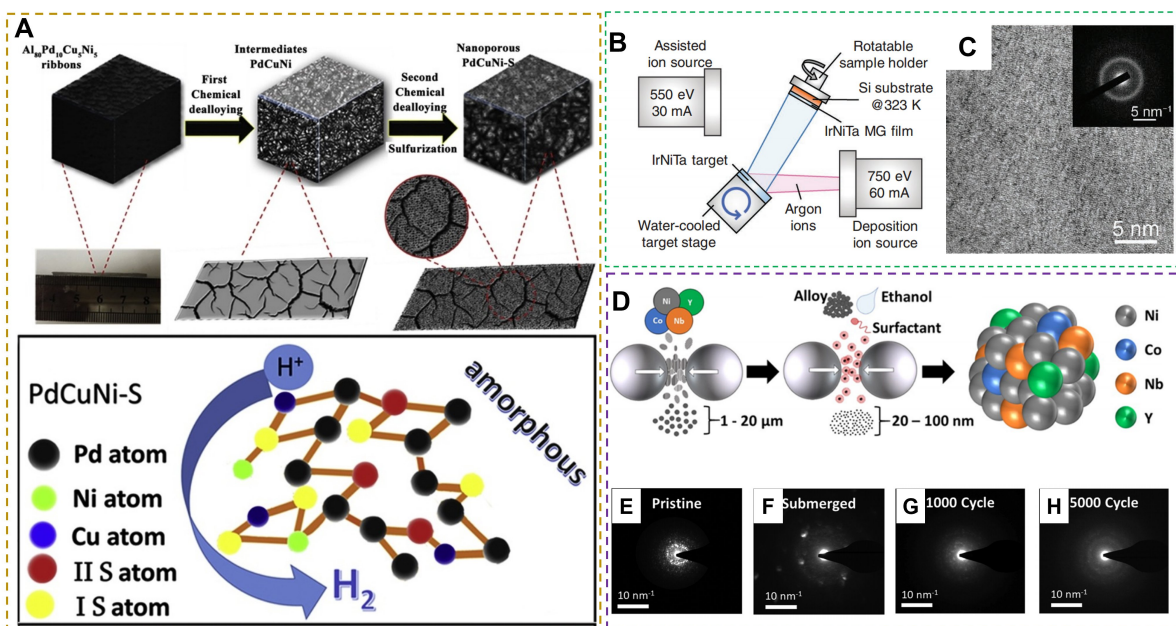
Figure 7. (A) Synthetic procedure of nanoporous PdCuNi-S catalyst. (Reproduced with permission[91]. Copyright 2019, Elsevier). (B) Schematic diagram of depositing $Ir_{25}Ni_{33}Ta_{42}$ MG film on Si substrates. (C) HRTEM image and its corresponding SAED pattern (inset) of the as-deposited $Ir_{25}Ni_{33}Ta_{42}$ MG film. (Reproduced with permission[93]. Copyright 2019, Wiley-VCH). (D) Schematic illustration of the two-stage ball milling synthesis process for producing amorphous nanoparticles. (E-H) Nanobeam diffraction (NBD) patterns at the surface regions in $Ni_{74.2}Co_5Nb_{12.5}Y_{8.3}$ nanoparticles. (Reproduced with permission[95]. Copyright 2020, American Chemical Society).

Ball milling method: A typical way to create amorphous catalysts and also known as mechanical alloying. This approach refers to conversing mechanical energy to the collision, friction, and shearing of solid feedstocks in a ball milling vessel; finally, the amorphous catalysts would be produced by mixing and reacting the feedstock powders at a tiny scale[94]. For instance, a two-stage ball milling process was used to prepare the amorphous $Ni_{79.2-x}Co_xNb_{12.5}Y_{8.3}$ (x = 0 and 5 at%) OER catalysts[95], and the precursor was the mixture of nickel (99.9 wt%, -100 mesh), cobalt (99.8 wt%, -100 mesh), niobium (99.99 wt%, -325 mesh), and yttrium (99.9 wt%, -40 mesh) metal element powders [Figure 7D]. The prepared amorphous catalysts deliver excellent structural stability [Figure 7E-H].

Based on the above description, we briefly summarize the preparation methods in Table 1.

Other novel methods

Based on the above analysis, the amorphous catalysts from most traditional methods face the issues of heterogeneity and uncontrollable texture. Hence, numerous novel preparation methods have been developed to obtain higher quality and stable amorphous catalysts. For example, the supersaturated precipitation method was applied to produce amorphous NiFeMo oxide with a mass of up to 515 g[96]. This method first mixes high-concentration metal chloride precursors (such as $NiCl_2 \cdot 2H_2O$ and $FeCl_3$) in water. Then, 1 M $Na_2MoO_4 \cdot 2H_2O$ aqueous solution was added to the mixture at ultrasonic conditions and reaction for 2 min; the samples were obtained via freeze-drying [Figure 8A]. Moreover, homogeneously mixing the high-temperature calcination-wet chemical synthesized highly crystalline $LaCoO_3$ ($LaCoO_3$-Pristine) nanopowders with urea in the mass ratio of 1:10, then heating at 450 °C for 2 h and cooling to room temperature can obtain reduced $LaCoO_3$ powder ($LaCoO_3$-Reduce) [Figure 8B][97]. The XRD pattern indicates the amorphous state of $LaCoO_3$-Reduce after reducing by urea [Figure 8C]. The disordered structure of $LaCoO_3$-Reduce in Figure 8D further demonstrates the amorphous character. Additionally, combining the merits of each preparation method is a new strategy to prepare amorphous catalysts. For example, amorphous TiO_2 nanofibers (a-TiO_2) were produced by combining the preparation methods of precursor solution[98], electrostatic spinning, and calcination [Figure 8E]. Moreover, combining hydrothermal with phosphating can synthesize $MoO_2/Ni_3(PO_4)_2$ self-supporting microcolumn electrocatalyst with amorphous MoOx phase at the NF surface (SA-$MoO_2/Ni_3(PO_4)_2$/NF)[99].

## CHARACTERIZATIONS OF AMORPHOUS CATALYSTS

The characterizations of amorphous catalysts can reveal the structure-activity relationship and then provide the experimental and theoretical basis for the design and applications of high-active stable amorphous electrocatalysts. Currently, the related characterizations can be divided into experiment and theory categories.

Experimental characterizations

A common characterization method of amorphous structures is XRD. The information on crystal structure and lattice parameters can be detected by the incident X-rays. However, the disordered crystal structure of amorphous induces steamed bun peaks occurring in XRD patterns[100,101], thus making it challenging to provide detailed structural information. Meanwhile, various amorphous catalysts always exhibit similar XRD patterns, resulting in the subtle differences between them indistinguishable via XRD. The micromorphology and fine structure of amorphous catalysts can be observed by TEM. The absence of clear lattice fringes in HRTEM means the disordered and irregular atomic arrangement in amorphous catalysts. The unit cell parameters or crystal face indexes cannot be deduced from HRTEM, which is different from crystalline catalysts. The diffraction ring or fuzzy core spots emerging in SAED can further verify the amorphous feature of catalysts. Similar to the crystalline catalysts, the band energy spectrum analysis from

**Table 1. Comparisons between three major preparation methods**

Methods	Liquid phase method	Vapor phase method	Solid phase method
Principle	Amorphous catalysts are formed by dissolving the desired atoms or molecules in a liquid solution to control reaction conditions	Materials are physically deposited onto a substrate in atomic or molecular form	Formation of amorphous catalyst materials under solid phase conditions by solid-state reactions
Applicable conditions	Usually performed at relatively low temperatures and pressures	Suitable for deposition at high temperatures; certain vacuum conditions	Synthesize some high melting point metals
Advantages	Simple operation; easily controlled reaction conditions	High homogeneity and controllability	Simple preparation; high controllability, *etc.*
Disadvantages	Difficulty in structural control; low purity	Require high temperature conditions and high equipment costs	High requirements on raw material composition and mixing uniformity
Categorizations	Sol-gel method: suitable for scenarios that require flexible control of ingredients and structure; Deposition method: suitable for preparing complex alloys or heterogeneous catalysts; Hydrothermal method: suitable for the preparation of hydroxides and hydroxide precursors to form particles or films of amorphous catalysts	PVD: typically used to prepare amorphous films with unique structures and excellent properties; CVD: preparation of amorphous catalysts with controlled gas phase composition and reaction conditions	Melt-quenching method: suitable for materials that require rapid cooling under high temperature conditions to form an amorphous structure; Sputtering method: suitable for controlled preparation of amorphous thin films under high vacuum conditions; Ball milling method: high-energy ball milling equipment and strict reaction environment control conditions are required
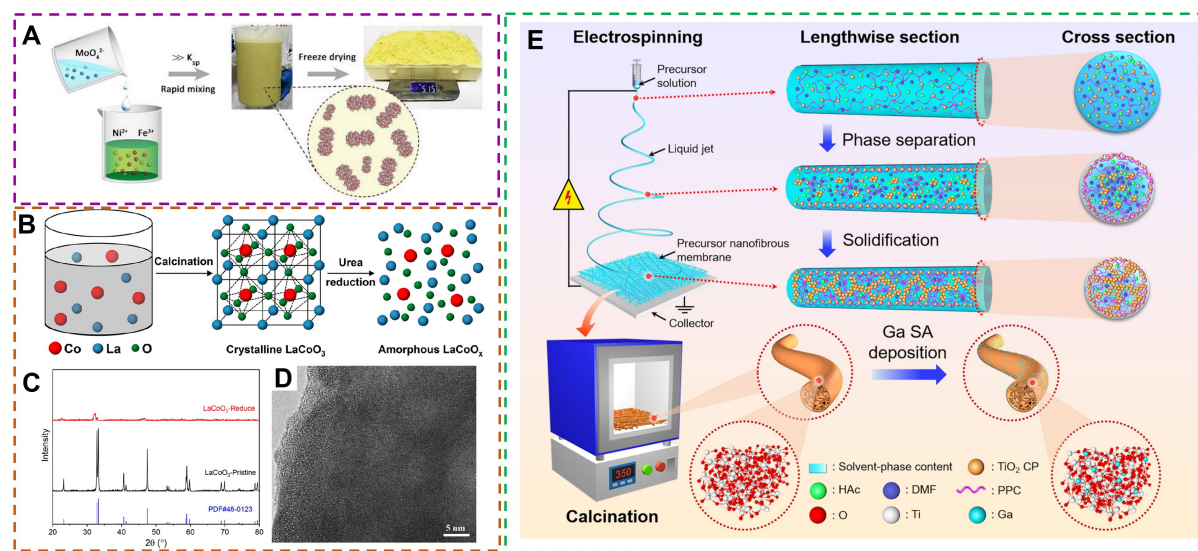
Figure 8. (A) The synthesis illustration of a-NiFeMo catalyst. (Reproduced with permission[96].Copyright 2019, Wiley-VCH). (B) The preparation schematic of crystalline $LaCoO_3$ and amorphous $LaCoO_x$ nanopowders. (C) XRD patterns of pristine and reduced $LaCoO_3$ nanopowders. (D) TEM image of reduced $LaCoO_3$ nanopowders. (Reproduced with permission[97].Copyright 2022, American Chemical Society). (E) The schematic diagram for the formation of lotus-root-like a-TiO_2 nanofibers and the atomic-scale deposition of Ga. (Reproduced with permission[98].Copyright 2022, American Chemical Society).

TEM can determine various element distributions in amorphous catalysts. Moreover, Zhan *et al.* reported that nanobeam electron diffraction (NBED) image of $(NbTiZr)_{77.8}Si_{22.2}$ (at.%) coating showed a broad diffraction ring indicating its amorphous nature [Figure 9A][102].

As an important characterization, X-ray absorption near-edge structure (XANES) is derived from X-ray absorption spectroscopy (XAS), which can detect more information in amorphous catalysts. Generally, the
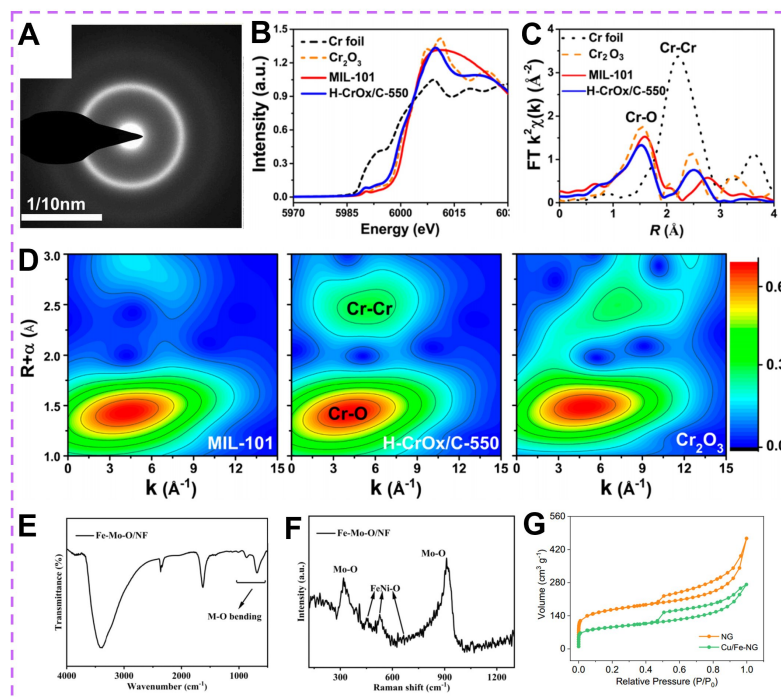
Figure 9. (A) The NBED pattern of $(NbTiZr)_{77.8}Si_{22.2}$ (at.%) coating. (Reproduced with permission[102]. Copyright 2022, Elsevier). (B) Cr K-edge XANES spectra and (C) Fourier-transforms of k3-weighted Cr K-edge EXAFS spectra in the R-space of H-CrO$_x$/C-550, MIL-101, commercial Cr_2O_3, and Cr foil. (D) Wavelet transforms for the k3-weighted EXAFS signals of MIL-101, H-CrO$_x$/C-550, and commercial Cr_2O_3. (Reproduced with permission[104]. Copyright 2022, American Chemical Society). (E) FTIR spectrum and (F) Raman spectrum of amorphous Fe-Mo-O/NF. (Reproduced with permission[105]. Copyright 2022, American Chemical Society). (G) N_2 adsorption-desorption isotherms of NG and Cu/Fe-NG. Copyright 2022. (Reproduced with permission[106]. Copyright 2020, American Chemical Society).

elemental oxidized state, coordination number, and chemical environment can be analyzed by the peak shape, position, intensity, and other characteristics of the XANES spectrum. For instance, the valence states of Mn in the original and oxygen-vacant samples were revealed by XANES, and they range between 3+ and 4+[103]. Compared with XANES, extended X-ray absorption fine structure (EXAFES) can provide more detailed information on interatomic distances and coordination numbers. The structural information on amorphous catalysts can be obtained by analyzing the background noise and vibrational characteristics in the EXAFES spectrum. For example, Pan *et al.* used XANES and EXAFES to explore the atomic coordination information in amorphous H-CrO$_x$/C-500 [Figure 9B and C][104]. The abundant coordination defects and oxygen vacancies in H-CrO$_x$/C-550 can be revealed by the Cr-O and Cr-Cr coordination bonds [Figure 9C], the fitting results and wavelet transforms (WT) of Cr K-edge EXAFS [Figure 9D]. Significantly, the intensity and oscillation amplitude decrease in XANES and EXAFS is associated with highly disordered/ amorphous structures. The presence of functional groups and short-range ordered structures of amorphous catalysts can be identified by Fourier transform infrared spectroscopy (FTIR) and Raman spectroscopy, respectively. For instance, the peaks at 860 and 685 cm^{-1} correspond to Fe(NiMo)-O [Figure 9E], while the peaks at 457, 529, and 664 cm^{-1} are associated with the vibration of FeNi-O in Fe-Ni oxide [Figure 9F][105], demonstrating the formation of amorphous Fe-Mo-O/NF. The specific surface area of amorphous catalysts can be measured by the N_2 adsorption-desorption curve. As displayed in Figure 9G, the specific surface areas of Cu nanoclusters/FeN$_4$ composites deposited on N-doped graphene (Cu/Fe-NG) and NG catalysts are 303.7 and 542.6 m^2 g^{-1}[106], respectively. Extensive research has been done to experimentally characterize amorphous catalysts, but their detailed crystal structures are still lacking, resulting in the relationship

between structure and performance remains unclear. Thus, developing advanced experimental characterizations to detect more information from amorphous catalysts is urgent. X-ray photoelectron spectroscopy (XPS) can characterize the chemical composition, surface chemical state and electronic structure of amorphous catalysts; monitor the surface changes during the reaction process and other aspects, which contributes to an in-depth understanding of amorphous catalysts in terms of their structure, surface reaction properties and catalytic performance. Electron energy loss spectroscopy (EELS) imaging, as a high-resolution, high-sensitivity, and non-destructive catalyst characterization technique, plays an important role in the study of the chemical composition, microstructure, electronic energy level distribution, and surface reactive sites of amorphous catalysts, which contributes to an in-depth understanding of amorphous catalysts. Based on the Cu valence state mapping of EELS spectral imaging, Chen *et al.* obtained that metallic Cu can be oxidized by SC CO_2 into amorphous Cu_xO, forming a structure with a core of Cu and an amorphous shell of Cu_xO[107].

Theoretical characterizations
Typically, the complicated properties of amorphous catalysts offer difficulty in capturing full information through experiments. The insufficient experimental characterizations provide a research platform for the development of theoretical characterizing amorphous catalysts. Machine learning (ML) can acquire the most representative feature from numerous data by automatically extracting and selecting features, thus improving its identifiability[108,109]. Combining numerous experimental data and simulation calculations, a model can be built to predict the structure of amorphous catalysts while designing and optimizing the structure by an optimization algorithm. For instance, the formation of amorphous Cu_xO was analyzed via ML [Figure 10] and can be roughly divided into three steps: surface oxidation, O penetration, and O departing[107].

DFT plays an important role in characterizing amorphous catalysts, and the main roles are summarized as follows. (1) The optimization of the potential energy surface can predict amorphous catalyst structures, such as atomic positions, crystal configuration, local environment, *etc.*[110]; (2) The movement of atoms and molecules in amorphous catalysts can be stimulated by molecular dynamics (MD) and other methods[111], thus revealing the dynamic process of catalytic reactions; (3) The catalytic activity of amorphous catalysts can be predicted by calculating the surface energy, adsorption properties, and energy-band structures; and (4) The electronic principles of amorphous catalysts in catalytic reactions can be revealed by calculating their electronic structural properties, such as electron density, energy band structure, density of states, *etc.* For example, He *et al.* modeled the formation mechanism of 2D amorphous $PtSe_x$ by using ab initio MD (AIMD) simulations based on DFT[112]. The $PtSe_2$ crystal structure with a $PtSe_x$ surface was obtained by sequentially removing Se atoms from the $PtSe_2$ monolayer and then calculating the selenium-depleted $PtSe_x$ monolayers to create an amorphous structure via AIMD. Moreover, the combination of ML and DFT can explore the complex structure-activity relationship in binary or ternary multi-metal (hydro)oxide amorphous catalysts[113].

MODIFICATION STRATEGIES OF AMORPHOUS CATALYSTS

Most amorphous catalysts feature the merits of numerous low-coordinating atoms, more randomly oriented unsaturated bonds, and flexible local structures, thus delivering excellent electrocatalytic activity. However, the large-scale applications of amorphous catalysts remain challenging. Therefore, numerous strategies have been developed to modify their compositions, defects, and surface properties, which are crucial for electrocatalytic reactions. The regulation strategies of amorphous catalysts can be summarized as structural design, composition tuning, surface modification, interfacial engineering, and electrochemical modification.
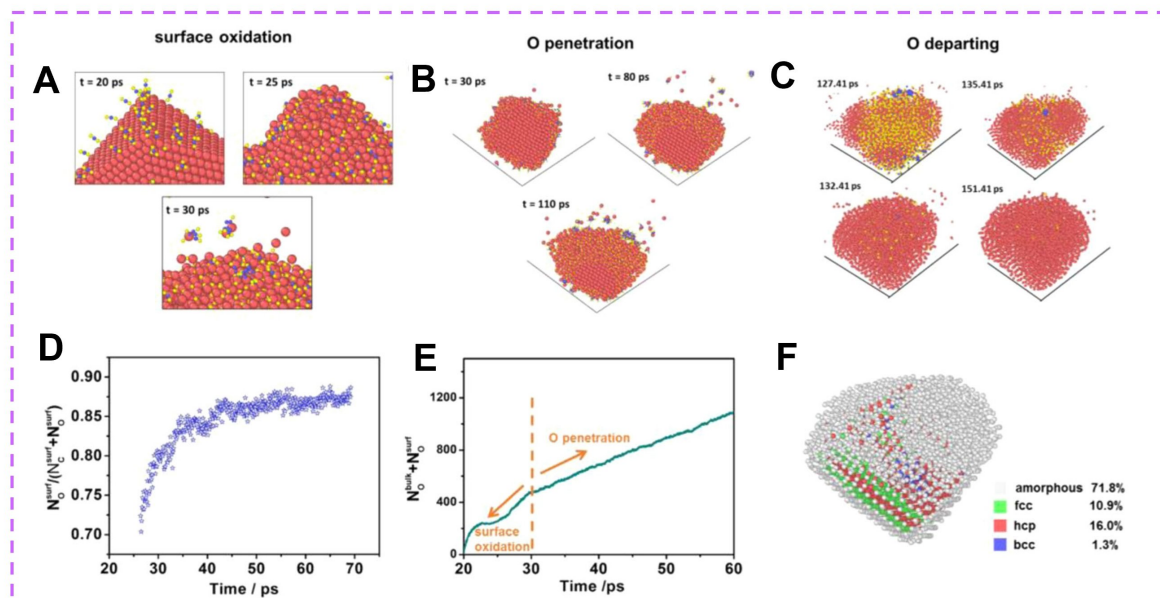
Figure 10. (A-F) The simulated mechanism for the amorphization. (Reproduced with permission[107]. Copyright 2023, Nature).

Structural design

An effective way to tune electrocatalytic properties is to develop innovative structural designs. The designed distinct structures can manipulate the inherent features of catalysts, such as electronic structures and mass transfer. At the same time, amorphous metal oxides with oxygen vacancies offer unique advantages for electrocatalysis. They provide high surface area, enhanced mass transport properties and tunable electronic structure, which facilitates efficient electrocatalytic processes[114]. For instance, single Ga atoms were distributed in the oxygen vacancies of lotus-root-like a-TiO$_2$ nanofibers (Ga-SA/a-TiO$_2$) [Figure 11A-C] to improve their selectivity for NRR[98]. The inset SAED indicates the amorphous nature of a-TiO$_2$ and Ga-SA/a-TiO$_2$, while the electron paramagnetic resonance (EPR) suggests the abundant oxygen vacancies in Ga-SA/a-TiO$_2$ [Figure 11D]. The obtained Ga-SA/a-TiO$_2$ delivers a high NH$_3$ yield (24.47 µg h^{-1} mg^{-1}) and high FE (48.64%) at a very low potential (-0.1 V$_{RHE}$) [Figure 11E], exhibiting excellent NRR performances. Moreover, the self-supporting NiFe- layered double hydroxide@Fe-MOF/iron foam-2 (NiFe-LDH@Fe-MOF/IF-2) OER electrocatalyst with a multi-level structure was prepared by *in-situ* Ni treatment to partially convert Fe-MOF into amorphous NiFe-LDH[115]. A TEM image [Figure 11F] shows that the structure of the NiFe-LDH@Fe-MOF/IF-2 catalyst is a flower-like structure composed of interconnected NSs. As shown in Figure 11G, amorphous NiFe-LDH was formed on the surface of Fe-MOF. Its unique hierarchical structure is conducive to exposing more active sites, shortening the diffusion path of charge carriers and increasing the rate of electron transfer, thus enhancing its catalytic performance. As displayed in Figure 11H and I, NiFe-LDH@Fe-MOF/IF-2 delivers a low OER overpotential of 183 mV and a Tafel slope of 41.16 mV dec^{-1} at 10 mA cm^{-2} in 1 M KOH solution.

Tuning the self-supported electrode structures can improve their catalytic properties. This can be mainly attributed to (1) Self-supporting system electrocatalytic materials are directly grown or anchored on the conductive substrate through a certain process without the need for adhesives, thus avoiding its inhibitory effect on the conductive ability of the material; (2) Most self-supporting substrates themselves have good electrical conductivity, which can effectively improve the electron transmission of electrocatalytic materials with poor conductivity and promote the effective transmission of carriers during the catalytic process; (3) A
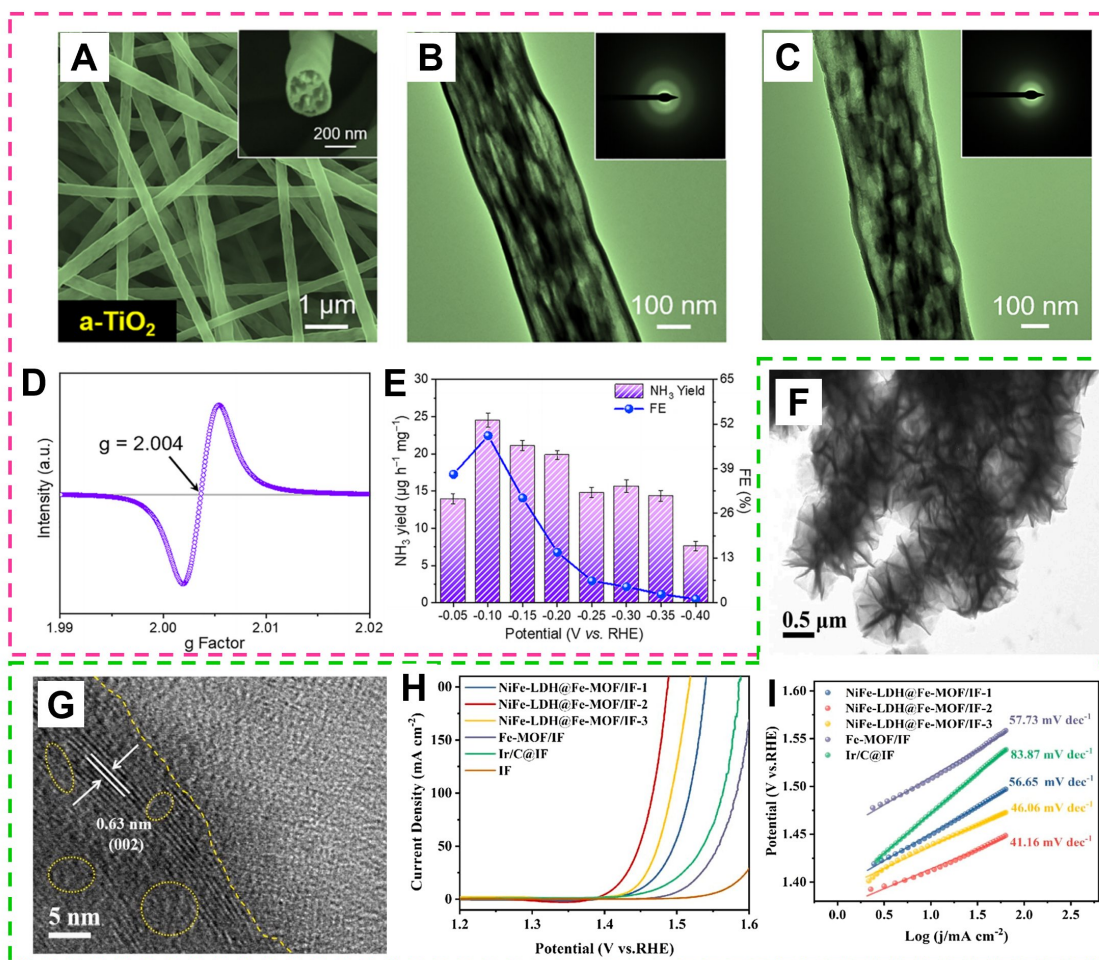
Figure 11. (A) SEM and (B) TEM images of a-TiO_2. (C) TEM image of Ga SA/a-TiO_2 nanofibers. (D) EPR spectra of Ga SA/a-TiO_2 nanofibers. (E) NH_3 yields and FEs of Ga SA/a-TiO_2 nanofibers at different potentials for 2 h (Reproduced with permission[98]. Copyright 2022, American Chemical Society). (F) TEM images and SAED pattern of NiFe-LDH@Fe-MOF/IF-2. (G) HRTEM image of NiFe-LDH@Fe-MOF/IF-2. (H) LSV curves of various samples. (I) Corresponding Tafel plots. (Reproduced with permission[115]. Copyright 2021, Elsevier).

strong interaction can be formed between the active material and the substrate. The strong contact interface between the electrocatalytic material and the self-supporting substrate can efficiently transport electrons and reduce the reaction barrier; and (4) Due to the strong contact between the electrocatalytic material and the self-supporting substrate, it avoids the shortcoming of easily falling off during the catalytic process using binders, so it shows good catalytic stability. For example, a self-supported amorphous $CoMoO_4$ nanowire array on Ti mesh ($CoMoO_4$ NWA/Ti) was produced by a simple two-step hydrothermal approach[116], which exhibits excellent HER activity and stability in 1 M KOH solution. Moreover, amorphous SA-MoO_2/Ni_3(PO_4)$_2$/NF with a self-supported 3D micropillar structure was prepared [Figure 12A and B] to catalytic HER[99]. The obtained catalysts featured an NF substrate with excellent electrical conductivity and a unique structure that increased the mass transfer rate and electrochemical surface area (ECSA) [Figure 12C], which further enhanced the electrical conductivity and thus accelerated the catalytic reaction. The surface amorphous state endows the SA-MoO_2/Ni_3(PO_4)$_2$/NF structure with self-repairing ability and improves its corrosion resistance [Figure 12D]. Meanwhile, the surface amorphous state can effectively
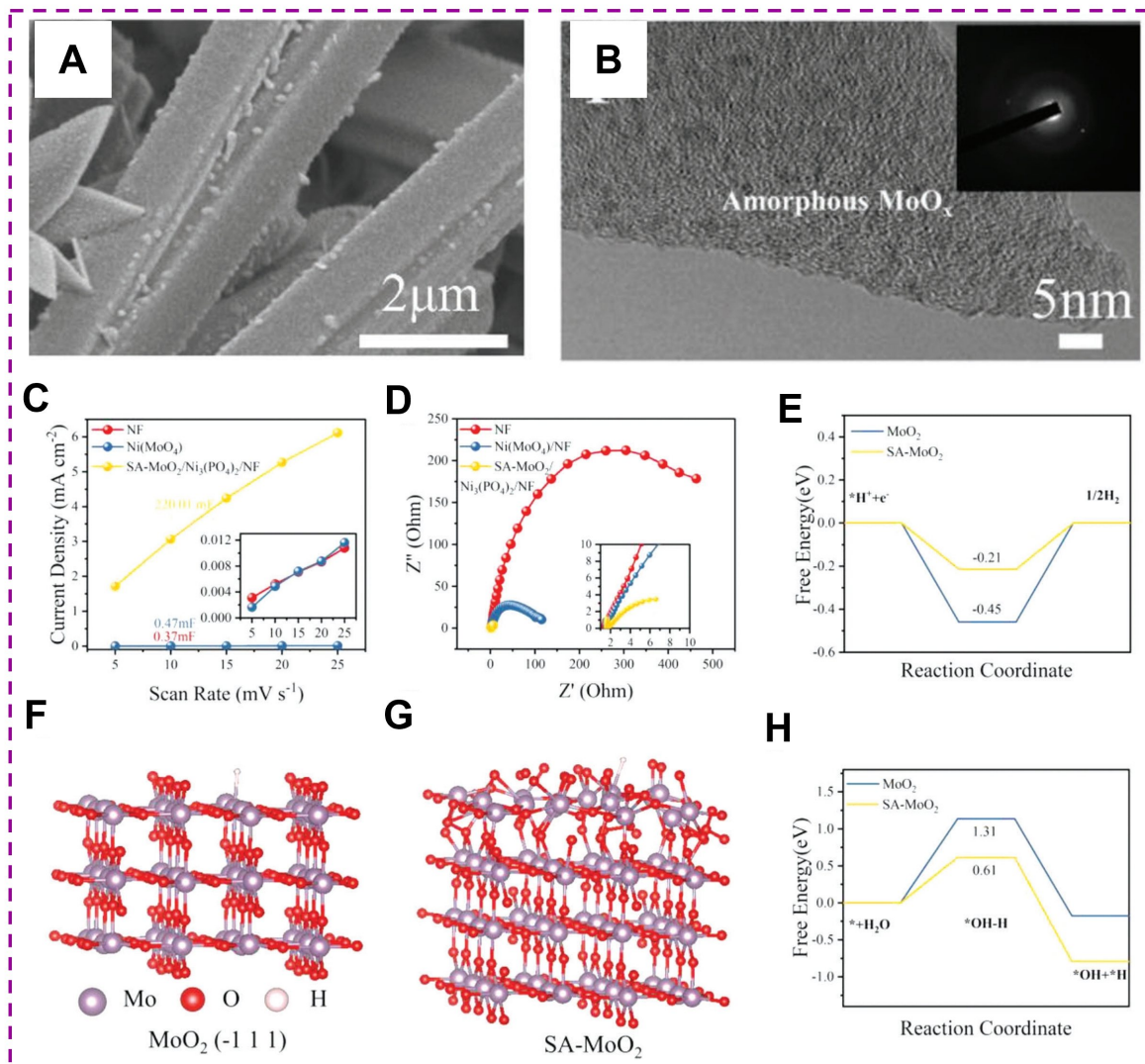
Figure 12. (A) SEM and (B) HRTEM images of $SA-MoO_2/Ni_3(PO_4)_2/NF$. (C) ECSA estimated by double-layer capacitance measurements. (D) Nyquist plots. DFT calculations: (E) Free energy of hydrogen adsorption. (F) Model of MoO_2 (-111) and (G) model of $SA-MoO_2$ (-111). (H) Energy barrier of water dissociation. (Reproduced with permission[99]. Copyright 2023, Wiley-VCH).

optimize the Gibbs free energy of hydrogen adsorption and the energy barrier of water decomposition [Figure 12E-H], thus exhibiting excellent electrocatalytic HER performances.

Composition tuning

The composition regulation can optimize the electronic structure and surface chemistry of the amorphous catalysts, generating active sites that facilitate electron transfer and improve conductivity, thus improving their catalytic activity and stability. The composition modification strategies include alloying, doping, and compounding. For instance, introducing Co^{2+} to amorphous MoS_X creates a Mo-S-Co structure[117], which increases active sites from unsaturated Mo atoms and S atoms, making it easier for electrons to migrate between the surface of the catalyst and the active sites, increasing the rate of electron transfer, and then improves its intrinsic electrocatalytic activity. Moreover, a novel amorphous P-doped MoS_2 nanocomposite was prepared by a facile hydrothermal method[118]. The obtained amorphous P-doped MoS_2 catalyst delivers

better catalytic activity and stability than that of the crystalline MoS_2 in acidic electrolytes. The Fe element was doped in amorphous Ni-P-B-O (NPBO) nanocages to prepare Fe-NPBO (FNPBO) catalysts and their amorphous feature was revealed via XRD patterns [Figure 13A][119]. The FNPBO, as an OER catalyst, exhibits a smaller overpotential and a smaller Tafel slope than that of NPBO [Figure 13B]. Amorphous $NiWO_4$ and Fe-doped $NiWO_4$ powders were prepared by the solution without or with $Fe(NO_3)_3 \cdot 6H_2O$, respectively [Figure 13C][120]. They show disordered structures [Figure 13D-G], and the electronic structure of $NiWO_4$ was tuned by Fe^{3+} doping [Figure 13H], improving electron transfer efficiency and further enhancing catalytic performance. The OER overpotential of the synthesized Fe-doped amorphous $NiWO_4$ exhibits a 90 mV drop than that of amorphous $NiWO_4$ at 10 mA cm^{-2} in 1.0 M KOH solution [Figure 13I]. The specific surface area of amorphous N, P, and F triple-doped $CoFe_2O_4$ was enlarged by attaching ultrafine MoS_2 nanoclusters on its surface. Since oxygen vacancies can affect the adsorption energy of intermediates, they change the reaction pathways, lower the reaction energy barriers, and improve the catalytic activity and selectivity of electrocatalysts. To further improve their activity, oxygen vacancies were created by using ionic liquids as dopants; thereby, the oxygen-vacancy-rich MoS_2/NPF-$CoFe_2O_4$ (MNC) catalysts were prepared[121]. As shown in Figure 13J, the absence of diffraction peaks in the XRD pattern signifies the amorphous feature of MNC. The numerous oxygen vacancies, amorphous structure, large surface area (148.9 m^2 g^{-1}), and active sites (such as N-Fe, N-Co, *etc.*) in MNC contribute to its superior OER performances, showing an overpotential of 250 mV and a Tafel slope of 41 mV dec^{-1} at 10 mA cm^{-2} [Figure 13K-M]. Furthermore, DFT simulations demonstrate that the presence of heteroatoms and MoS_2 can tune the electronic structure and lower the energy barrier of the intermediates during the OER process [Figure 13N].

Per the above analysis, composition tuning can significantly improve the catalytic properties of catalysts. On the one hand, the adjustment of the catalyst composition can expand the reaction types, thus realizing various reactions via catalyst design and preparation. Catalysts with varied compositions have distinct chemical characteristics, surface structures, and crystal structures that allow them to be applied to a range of reactants and reaction conditions while enhancing catalytic activity. On the other hand, tuning the ratio and distribution of catalyst components can regulate crystal structure, coordination environment, electronic structure, and other surface properties, thus exposing more active sites while optimizing their adsorption and reaction properties, which, in turn, reduces charge transport paths and losses, accelerates charge transfer efficiency, and improves the conductivity of the material itself. Finally, the tuned composition can limit phase transitions and lattice flaws occurring in catalysts and then reduce catalyst deactivation during the reaction process and exhibit excellent catalytic stability.

Surface modification

The factors of the electronic structure and surface acid-base properties that affect the catalytic reactions of amorphous catalysts can be controlled by surface modification. For example, the microstructure of amorphous FNPBO can be adjusted by various Fe/Ni ratios [Figure 14A-F][119]. The microstructure changes from nanocages to NSs as the Fe/Ni ratio in FNPBO increases, thus altering its OER performance. The optimized FNPBO ($Fe_{6.4}Ni_{16.1}P_{12.9}B_{4.3}O_{60.2}$) delivers excellent OER activity of 236 mV overpotential and 39 mV dec^{-1} Tafel slope at 10 mA cm^{-2} and can continuously operate for 50 h at 236 mV without attenuation [Figure 14G and H]. The amorphous mixed-metal (Ni-Fe) hydroxide nanostructures with uniform Ni/Fe distribution and controllable Ni/Fe ratios were prepared by Gao *et al.* and used as highly efficient OER electrocatalysts[122]. The catalytic performances of amorphous Ni-Fe hydroxides and their Ni content exhibit a volcano relationship, indicating the vital for generating excellent alloy hydroxide/oxide OER catalysts is their composition. The highly disordered structures and irregular surfaces endow amorphous $Ni_{0.71}Fe_{0.29}(OH)_x$ catalysts with more active site exposure and enhanced charge transfer efficiency. Moreover, a self-assembled amorphous molybdenum oxide-loaded single-atom Ru catalyst (Ru-SAs-MoO_{3-x}/NF) was
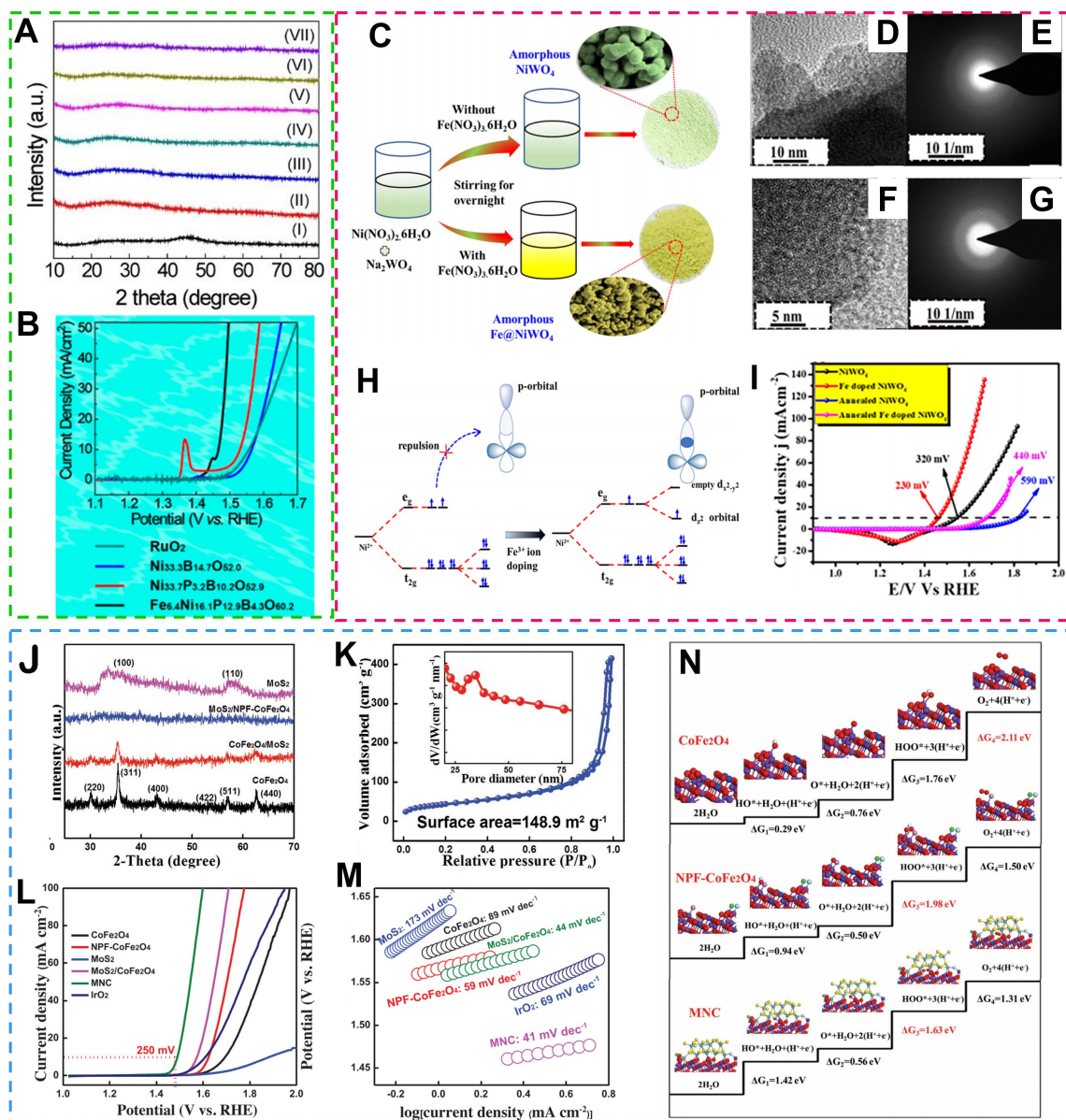
Figure 13. (A) XRD patterns of the FNPBO products with different ratios of Fe to Ni. (B) LSV curves of different samples. (Reproduced with permission[119]. Copyright 2019, American Chemical Society). (C) The synthesis of systematic amorphous $NiWO_4$ and Fe-doped amorphous $NiWO_4$. (D) HRTEM and (E) SAED of $NiWO_4$. (F) HRTEM and (G) SAED of Fe-doped $NiWO_4$. (H) Possible crystal field study of $NiWO_4$ with or without Fe^{3+} doping. (I) Backward LSV curve of $NiWO_4$, Fe-doped $NiWO_4$, annealed $NiWO_4$, and annealed Fe-doped $NiWO_4$ at a scan rate of 5 mV/s in 1 M KOH. (Reproduced with permission[120]. Copyright 2023, American Chemical Society). (J) XRD patterns of the prepared catalysts. (K) N_2 adsorption-desorption isotherm and pore-size distribution (inset) of the MNC. (L) OER polarization curves without *iR*-compensation. (M) Tafel slopes. (N) The elementary steps for the OER process catalyzed by various catalysts. (Reproduced with permission[121]. Copyright 2018, WILEY-VCH).

reported by Feng *et al*.[78]. The obtained Ru SAs-MoO$_{3-x}$/NF features a 3D flower-like structure, amorphous features, and uniform distributed Ru monoatoms, which endow the catalyst with a large surface area and numerous active centers, enhancing the charge transfer rate. Finally, it facilitates the mass-transfer kinetics of electrochemical water decomposition.
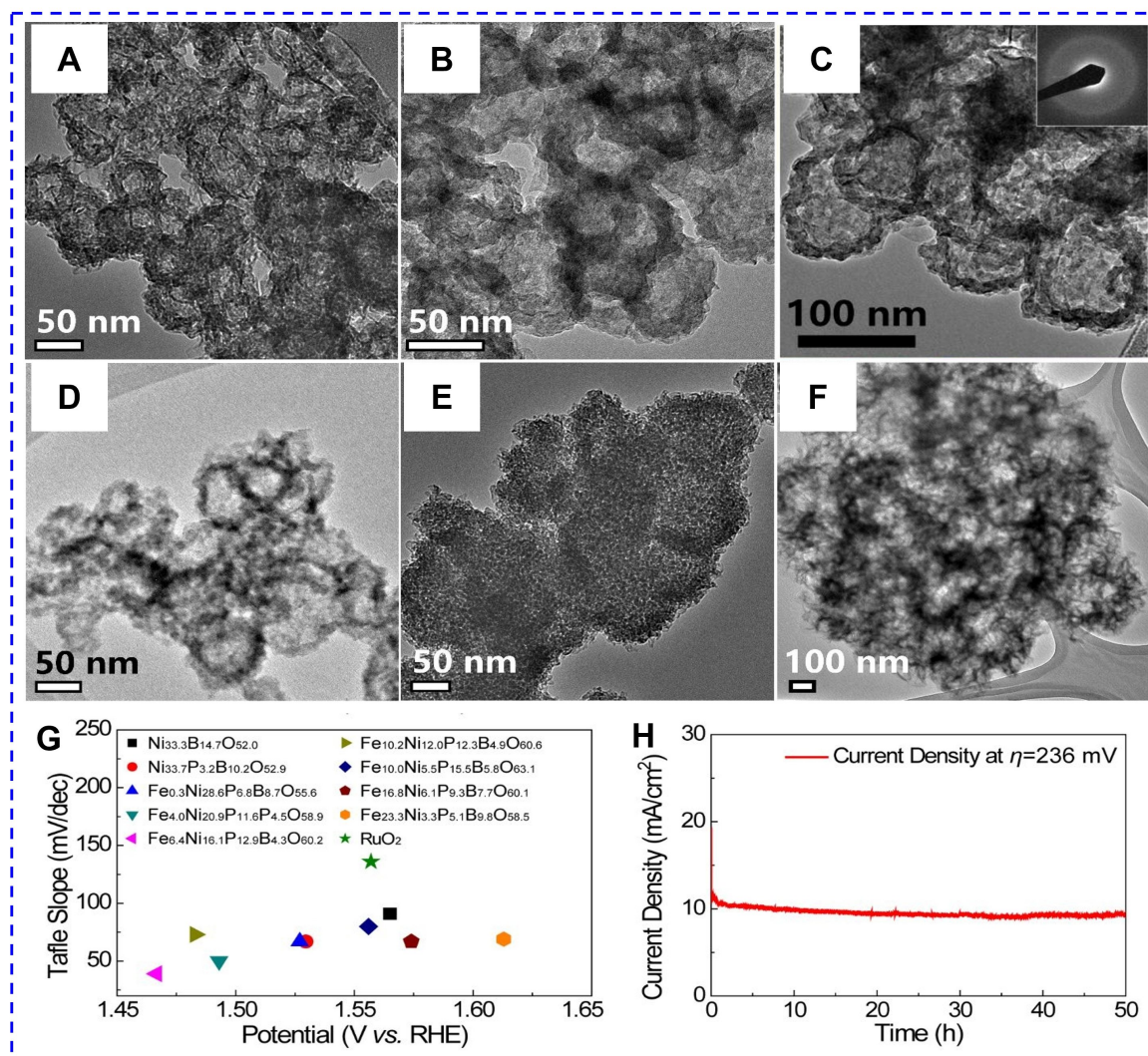
Figure 14. TEM of FNPBO with different Fe/Ni ratios: (A) $Fe_{0.3}Ni_{28.6}P_{6.8}B_{8.7}O_{55.6}$; (B) $Fe_{4.0}Ni_{20.9}P_{11.6}P_{4.5}O_{58.9}$; (C) $Fe_{6.4}Ni_{16.1}P_{12.9}B_{4.3}O_{60.2}$ (the insert is SAED pattern); (D) $Fe_{10.2}Ni_{12.0}P_{12.3}B_{4.9}O_{60.6}$; (E) $Fe_{10.0}Ni_{5.5}P_{15.5}B_{5.8}O_{63.1}$; and (F) $Fe_{16.8}Ni_{6.1}P_{9.3}B_{7.7}O_{60.1}$. (G) Tafel slope-potential plots of the $Ni_{33.3}B_{14.7}O_{52.0}$, $Ni_{33.7}P_{3.2}B_{10.2}O_{52.9}$, FNPBO catalysts, and commercial RuO_2. (H) Durability test of $Fe_{6.4}Ni_{16.1}P_{12.9}B_{4.3}O_{60.2}$ nanocages at 236 mV. (Reproduced with permission[119]. (Copyright 2019, American Chemical Society).

Interfacial engineering

The optimization of the interaction between amorphous catalysts and reactants, the improvement of the catalyst surface activity, and the regulation of surface active centers and adsorption sites can be realized by interfacial engineering, thus selectively modulating various reactions. Meanwhile, the microcrystalline regions present in the amorphous catalysts can influence the electrocatalytic performance of the materials, which is due to the fact that the coexistence of the crystalline and amorphous phases can provide a richer surface structure, increase the density of active sites, and improve the reactivity of the catalysts; modulate the surface energy of the catalysts, which makes the reactants easier to be adsorbed and transformed; improve the charge transport performance of the catalysts, reduce the resistance, and increase the electron transport rate, thus accelerating the reaction rate; and increase the stability and resistance to loss of activity, which prolongs the service life of the catalysts. For instance, a new amorphous/crystalline CrO_x-Ni_3N with heterostructure was grown on NF via the combination of hydrothermal and nitridation[123]. The DFT calculations indicate that the electronic structure modulation at the CrO_x-Ni_3N interface is conducive to

optimizing H_2O dissociation (ΔG_{H-OH}) and H adsorption (ΔG_H), thus, in turn, contributing to excellent and stable HER properties [Figure 15A]. Meanwhile, CrO_x-Ni_3N delivers a higher electron density near the Fermi energy level than that of Ni_3N, suggesting its improved conductivity [Figure 15B]. The CrO_x-Ni_3N heterostructure shows nanoparticles decorated NS structure [Figure 15C] and exhibits mixed phases; the nanoparticles are crystalline Ni_3N, while the NSs are amorphous CrO_x [Figure 15D]. The abundant oxygen vacancies and amorphous/crystalline interfaces endow CrO_x-Ni_3N catalysts with more active site exposure and increased intrinsic activity, resulting in excellent HER performances. Moreover, the $CoFeO_x(OH)_y$/$CoO_x(OH)_y$ (CFOH/COH) was prepared by coupling various $CoFeO_x(OH)_y$ with $CoO_x(OH)_y$[124], which exhibits a unique amorphous core-shell structure. The overpotential of CFOH/COH catalysts is smaller than A-F and A-C catalysts at the same current density, indicating that the amorphous core/shell structure was indeed conducive to increasing HER activity and accelerating electron transfer rate between the catalyst interface and electrolyte. The optimized CFOH/COH-1 (the ratio of Co/Fe is 1:1) catalyst delivers better catalytic activity than others [Figure 15E]. The nanoflower-like heterostructure amorphous $NiFe(OH)_x$/crystalline (Ni, Fe)Se on the NF catalyst was designed by Sun *et al.* and used electrocatalytic water splitting [Figure 15F-J][125]. The amorphous $NiFe(OH)_x$ features more active site exposure and a super-hydrophilic interface, facilitating electrolyte contact with the catalyst and the release of gas bubbles. The interfacial electronic interactions between amorphous and crystalline phases can modulate the catalyst's electronic structure and optimize intermediate conversion, increasing the electrical conductivity and thus accelerating catalytic kinetics.

In short, catalyst interfacial engineering can create heterogeneous structures forming microcrystalline regions and significantly increase catalytic activity. The first reason is that the formed heterogeneous structure exposes more active sites and expands the reaction boundary area, thus enhancing the activity at the electrolyte-electrode interfaces. Another reason is that heterostructures can modulate catalyst electronic structures and then improve catalytic activity. The heterostructure interfaces of different materials can provide various lattice structures, change local potentials, modulate electronic states, alter energy levels, and tune catalyst surface active sites, thereby enhancing the charge transfer rate and improving the material conductivity. Finally, the formed amorphous interfaces reduce local stress and dislocation density in crystals, decrease the formation and diffusion of lattice defects, and prevent surface oxidation and corrosion, thus improving the adaptability and long-term stability of catalysts.

Electrochemical modification

The potentials or currents are conducted to electrochemical modulate amorphous catalysts, thus activating the catalyst surface or modulating the electrocatalytic process. The introduction of activatable functional groups, such as hydroxyl and carboxyl groups, on the surface of amorphous catalysts by electrochemical methods can increase the active sites of the catalysts and improve the reactivity; optimize the paths and rates of electron transport and improve the conductivity. For example, the amorphous high-entropy CoNiFeMn phosphorus oxide (CNFMPO) [Figure 16A] was obtained by a simple low-potential electrodeposition method[126]. The HER-activated CNFMPO undergoes surface reconstruction; during the activation process, the NS layer gradually shrinks and thickens for surface dissolution and redeposition of metal salts. Similarly, OER-activated CNFMPO undergoes surface reconstruction; the surface elements, phosphite, and phosphate at high valence experience dissolution and redeposition, resulting in the NSs gradually transforming into fine nanoparticles and reconstructing into oxides or (oxy)hydroxides. Compared with the reference samples, these structural changes endow the activated CNFMPO catalyst electrode with a faster electron transfer rate, an increased electrochemically active surface area, and more active sites, delivering excellent HER and OER properties in 1 M KOH solution [Figure 16B and C]. Moreover, the amorphous small $Sn(HPO_4)_2$ (SnP) nanoparticles were prepared by Cheng *et al.* from a hydrothermal method[127]. Placing SnP in a CO_2-saturated 1.0 M KOH solution and applying a negative potential (0.7 V_{RHE}) to conduct *in situ*
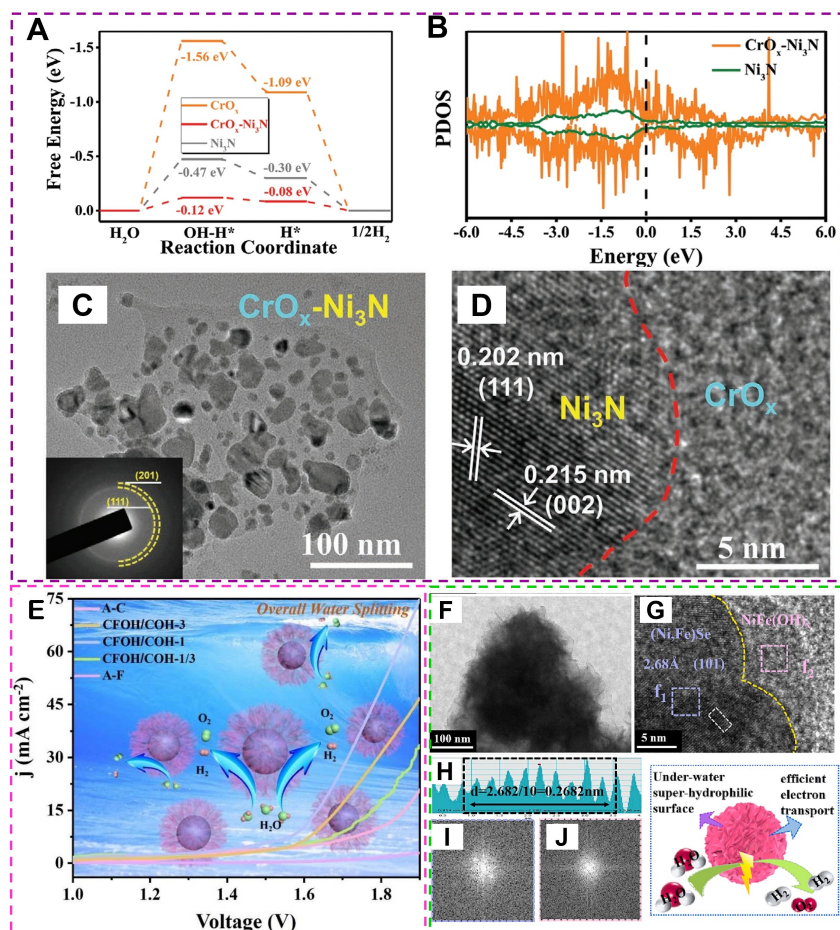
Figure 15. (A) The calculated Gibbs free energy of OH-H and H adsorption for the Ni_3N, CrO_x, and CrO_x-Ni_3N. (B) The total PDOSs of the Ni_3N and CrO_x-Ni_3N. (C and D) TEM characterizations of CrO_x-Ni_3N. (Reproduced with permission[123]. Copyright 2022, Wiley-VCH). (E) Schematic illustration of the overall water splitting process. Amorphous CFOH/COH catalyst exhibits much better performances than other as-synthesized A-F or A-C catalysts. (Reproduced with permission[124]. Copyright 2020, Elsevier). (F and G) TEM and HRTEM of NFSe@NFOH/NF. (I and J) Corresponding FFT patterns of the selected regions marked by purple and pink squares, respectively. (H) Lattice spacing corresponds to the selected white region. (Reproduced with permission[125]. Copyright 2023, Elsevier).

electrochemical reconstruction and form a core-shell P-Sn/SnO$_x$ structure electrode [Figure 16D and E]. The presence of amorphous SnO$_x$ layers and surface phosphorus species suppresses the HER and contributes to the current density and stability of CO$_2$RR. The theoretical results demonstrate that the embedded surface P species and adsorbed phosphoric acid groups effectively contribute to forming formate rather than other products [Figure 16F-I].

From the above examples, the main reasons for how electrochemical modification improves electrocatalyst catalytic activity can be summarized as follows. (1) Regulating electronic states: The applied voltage can tune the surface-distributed electrons of electrocatalysts, the electron density of active sites, and the adsorption characteristics of reactants. Generally, applying a positive potential can expose more surface active sites and improve the adsorption/activation efficiency of reactants, thus enhancing the catalytic activity; (2) Improvement of charge transport: Modulation of the electron transport properties of amorphous catalysts to reduce resistance, increase electron transport rate, and enhance conductivity; (3)
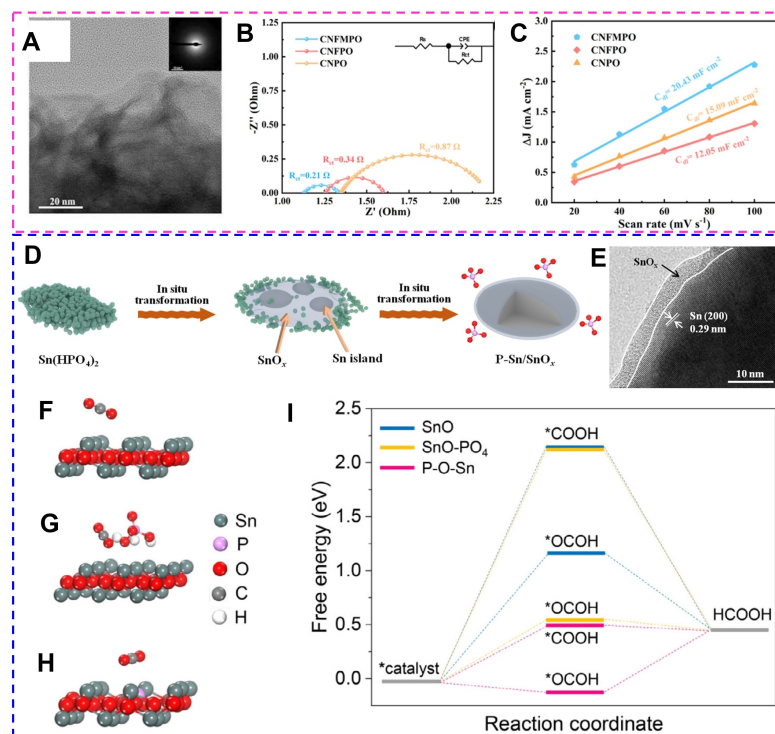
Figure 16. (A) TEM images of CNFMPO (inset is SAED). (B) EIS Nyquist plots of HER-activated electrodes. (C) Plots of capacitive current as a function of scan rates for OER-activated electrodes. (Reproduced with permission[126].Copyright 2024, Elsevier). (D) A proposed *in situ* derivatization process. (E) HRTEM images of SnP after CO_2RR. (F-I) Adsorption configurations of CO_2 on the surfaces of SnO (F), $SnO-PO_4$ (G), and P-O-Sn (H). (I) Free energy diagram of CO_2RR to HCOOH. (Reproduced with permission[127].Copyright 2023, Elsevier).

Promoting reaction kinetics: The potential of reactants can be adjusted by applying an external potential, and then changing the activation energy and reaction rate constant. Commonly, the applied proper potential facilitates high-energy intermediates or atomically active states to form on the catalyst surfaces, thus lowering the activation energy of reactants and increasing the reaction rate; and (4) Modulating surface adsorption energy: The exerted applied potential can change the catalyst surface distributed charge and regulate the surface reactant adsorption strength. The increased adsorption sites and moderate adsorption strength can optimize the reactant adsorption and activation states on catalyst surfaces, finally improving catalytic activity.

APPLICATIONS OF AMORPHOUS CATALYSTS IN ELECTROCATALYSIS

The large specific surface area, high catalytic activity, good electron conductivity, and structural durability enable amorphous materials to be widely applied in electrocatalysis. As illustrated in Figure 17, the main research progress of amorphous materials in electrocatalysis is briefly summarized, and their applications in HER, OER, ORR, Co_2RR, and NRR are mainly introduced as follows[128-139].

HER

As a crucial half-reaction in electrocatalytic water splitting, HER plays a pivotal role in sustainable energy conversion and storage fields[140-142]. This reaction involves a two-electron transfer process, and its pathways can be classified as the Volmer-Heyrovsky process (always used in electrochemical desorption mechanism) and the Volmer-Tafel process (commonly applied in recombinant desorption mechanism). The formation
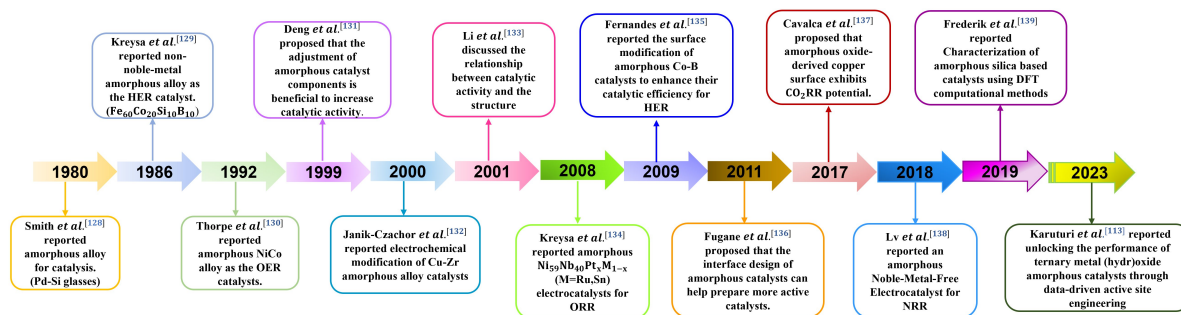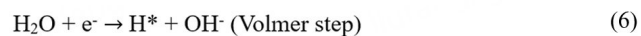
Figure 17. The main research progress of amorphous materials in electrocatalysis.

of hydrogen intermediate (H*) is expressed in the following Equations (3-8), which are substantially influenced by the pH of the electrolyte[141].

In acidic media:

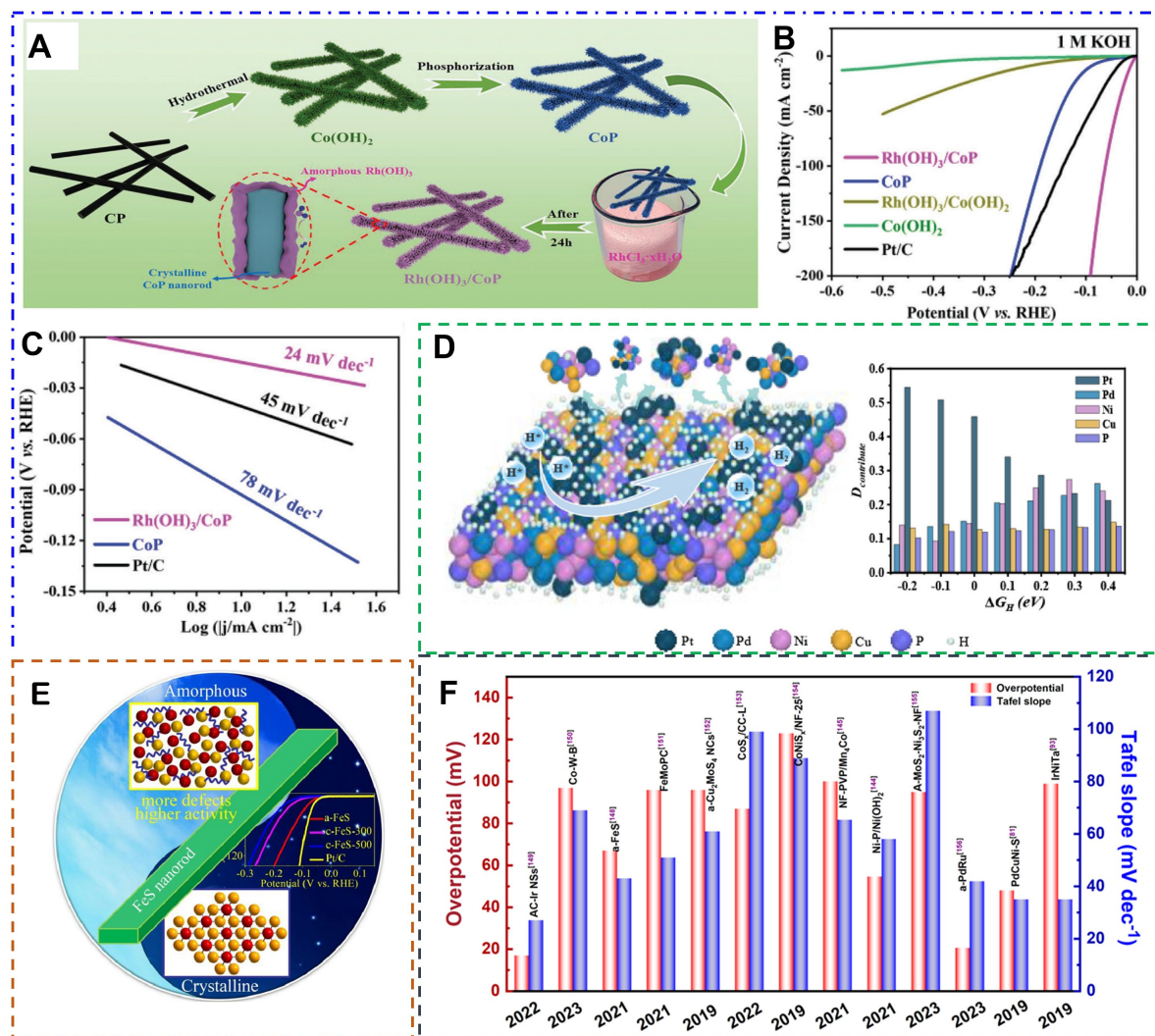$$H^+ + e^- \rightarrow H^* \text{ (Volmer step)} \tag{3}$$

$$H^+ + e^- + H^* \rightarrow H_2 \text{ (Heyrovsky step)} \tag{4}$$

$$H^* + H^* \rightarrow H_2 \text{ (Tafel step)} \tag{5}$$

In alkaline media:

$$H_2O + e^- \rightarrow H^* + OH^- \text{ (Volmer step)} \tag{6}$$

$$H_2O + e^- + H^* \rightarrow H_2 + OH^- \text{ (Heyrovsky step)} \tag{7}$$

$$H^* + H^* \rightarrow H_2 \text{ (Tafel step)} \tag{8}$$

The HER mechanism typically contains the steps of electron transfer, atomic rearrangement, intermediate species formation and dissociation, *etc*. In detail, the hydrogen ions on the cathode surface receive electrons and form hydrogen atoms (H*), and then, two H* integrate to form H_2 molecules[143]. The occurrence of HER needs to introduce catalysts that can reduce activation energy and accelerate reaction kinetics. In the currently studied electrocatalysts, amorphous catalysts feature the advantages of high activity, uniform loading, low catalyst deactivation rate, and tunability, receiving wide applications in HER.

For example, amorphous/crystalline $Rh(OH)_3$/CoP heterostructure was constructed to catalyze HER in the entire pH range [Figure 18A][144]. In 1.0 M KOH solution, $Rh(OH)_3$/CoP delivers a lower overpotential of 13 mV and Tafel slope of 24 mV dec^{-1} at 10 mA cm^{-2}, and the HER activity surpasses other comparison samples [Figure 18B and C]. This can be attributed to the unique heterostructure of $Rh(OH)_3$/CoP, which has special hydrophilic/aerophobic properties, accelerates mass transfer, and provides abundant exposed active sites and appropriate defects. A distinctive fiber-like porous amorphous NF-PVP/Mn_xCo_y was prepared to reduce water[145], which benefits gas diffusion and the interaction between the catalyst and electrolyte solution. The optimized amorphous NF-PVP/Mn_4Co NSs exhibit a low overpotential of 100 mV at 10 mA cm^{-2}, showing great potential in HER at a large scale. The HER activity of amorphous RuS_2 is superior to that of crystalline RuS_2, delivering a lower overpotential of 141 mV and a Tafel slope of 65.6 mV dec^{-1} at 10 mA cm^{-2}[146]. Moreover, the ML was conducted to calculate H adsorption Gibbs free energy (ΔG_H),

Figure 18. (A) Synthesis illustration of the Rh(OH)$_3$/CoP. Electrocatalytic HER performance in 1 M KOH solution. (B) HER polarization curves, (C) Tafel plots. (Reproduced with permission[144]. Copyright 2023, Wiley-VCH). (D) H-metal distance contribution analysis as the function of ΔG_H. (Reproduced with permission[147]. Copyright 2023, Elsevier). (E) LSV polarization curves for the HER of different catalysts. (Reproduced with permission[148]. Copyright 2021, Elsevier). (F) The electrocatalytic HER properties of the recent amorphous catalysts.

and then screen and analyze the optimal active sites from the established 11,752 models[147]. The optimal ratio of Pt:Pd:Ni:Cu:P = 0.33:0.17:0.155:0.16:0.185 was acquired for the local chemical environment, confirming the adsorption clusters of Pt, Pd, and Ni atoms are the main factors determining catalytic performances [Figure 18D]. In detail, Pt atoms are favorable to reducing ΔG_H while Pd and Ni atoms are favorable to increasing ΔG_H; they synergistically regulate the catalytic activity of adsorption clusters. The amorphous Fe$_{0.95}$S$_{1.05}$ (a-FeS) nanorod catalysts were prepared to catalyze HER and showed excellent electrocatalytic activity[148]. A low overpotential of 67 mV was obtained at 10 mA cm^{-2} and can stably operate for 80 h, outperforming other crystal electrocatalysts [Figure 18E]. Moreover, the electrocatalytic HER properties of the recent amorphous catalysts are summarized in Figure 18F[149-156].

For example, amorphous/crystalline Rh(OH)$_3$/CoP heterostructure was constructed to catalyze HER in the entire pH range [Figure 18A][144]. In 1.0 M KOH solution, Rh(OH)$_3$/CoP delivers a lower overpotential of 13 mV and Tafel slope of 24 mV dec^{-1} at 10 mA cm^{-2}, and the HER activity surpasses other comparison samples [Figure 18B and C]. This can be attributed to the unique heterostructure of Rh(OH)$_3$/CoP, which has special hydrophilic/aerophobic properties, accelerates mass transfer, and provides abundant exposed active sites and appropriate defects. A distinctive fiber-like porous amorphous NF-PVP/Mn$_x$Co$_y$ was prepared to reduce water[145], which benefits gas diffusion and the interaction between the catalyst and electrolyte solution. The optimized amorphous NF-PVP/Mn$_4$Co NSs exhibit a low overpotential of 100 mV at 10 mA cm^{-2}, showing great potential in HER at a large scale. The HER activity of amorphous RuS$_2$ is superior to that of crystalline RuS$_2$, delivering a lower overpotential of 141 mV and a Tafel slope of 65.6 mV dec^{-1} at 10 mA cm^{-2}[146]. Moreover, the ML was conducted to calculate H adsorption Gibbs free energy (ΔG_H),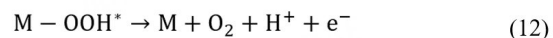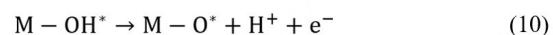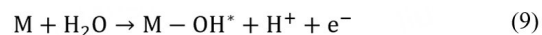 and then screen and analyze the optimal active sites from the established 11,752 models[147]. The optimal ratio of Pt:Pd:Ni:Cu:P = 0.33:0.17:0.155:0.16:0.185 was acquired for the local chemical environment, confirming the adsorption clusters of Pt, Pd, and Ni atoms are the main factors determining catalytic performances [Figure 18D]. In detail, Pt atoms are favorable to reducing ΔG_H while Pd and Ni atoms are favorable to increasing ΔG_H; they synergistically regulate the catalytic activity of adsorption clusters. The amorphous Fe$_{0.95}$S$_{1.05}$ (a-FeS) nanorod catalysts were prepared to catalyze HER and showed excellent electrocatalytic activity[148]. A low overpotential of 67 mV was obtained at 10 mA cm^{-2} and can stably operate for 80 h, outperforming other crystal electrocatalysts [Figure 18E]. Moreover, the electrocatalytic HER properties of the recent amorphous catalysts are summarized in Figure 18F[149-156].

OER

For water splitting, another key half-reaction is OER. However, the four-electron transfer involved in OER leads to a great challenge in improving overall water-splitting kinetics. The commonly accepted OER mechanism at acidic (Equations 9-12) or alkaline (Equations 13-16) conditions includes the following four steps, respectively[157]. The OER operates in acidic or alkaline solutions, both involving the formation of OH*, O*, and OOH* intermediates. The specific reaction pathways and kinetics of OER highly depend on the binding strength of M-OH*, M-O*, or M-OOH*[158].

In acidic media:

$$M + H_2O \rightarrow M - OH^* + H^+ + e^- \qquad (9)$$

$$M - OH^* \rightarrow M - O^* + H^+ + e^- \qquad (10)$$

$$M - O^* + H_2O \rightarrow M - OOH^* + H^+ + e^- \qquad (11)$$

$$M - OOH^* \rightarrow M + O_2 + H^+ + e^- \qquad (12)$$

In alkaline media:

$$M + OH^- \rightarrow M - OH^* + e^- \qquad (13)$$

$$M - OH^* + OH^- \rightarrow M - O^* + H_2O + e^- \qquad (14)$$

$$M - O^* + OH^- \rightarrow M - OOH^* + e^- \qquad (15)$$

$$M - OOH^* + OH^- \rightarrow M + O_2 + H_2O + e^- \qquad (16)$$
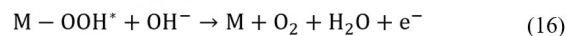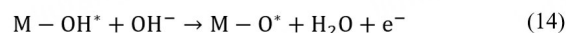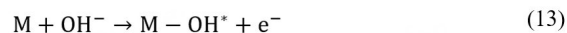
Effective electrocatalysts play a crucial role in driving water splitting. As previously reported electrocatalysts, amorphous catalysts show unparalleled advantages in electrocatalyzing OER and are receiving increasing

attention. For instance, hollow multichannel amorphous NiFe nanoreactors (NiFe-ANR) were produced as OER electrocatalysts[159], and their performances overmatch those of crystalline nanoreactor and amorphous non-nanoreactor catalysts. The amorphous structure enables NiFe-ANR to oxidize and form high-valent reactive species; meanwhile, numerous microcrystalline interfaces provide more active sites. Furthermore, the nanoreactor structure causes a localized high hydroxide concentration in NiFe-ANR and effectively promotes OER. As a result, the overpotential of NiFe-ANR (228 mV) is 118 mV lower than NiFe-CNR and 75 mV lower than NiFe-ANR at 10 mA cm^{-2}. A pervasive top-down strategy was developed by Liu *et al.* to prepare amorphous oxide materials by low-temperature treating chalcogenide hydroxides [Figure 19A], which is capable of amorphizing a variety of unitary, binary, and ternary chalcogenide hydroxides[160]. The current density of the obtained ternary FeCoSn(OH)$_6$-300 amorphous oxide reaches 178 mA cm^{-2} at 1.6 V$_{RHE}$ and stably operates for 200 h at 100 mA cm^{-2} [Figure 19B and C], which surpasses many previously reported OER electrocatalysts. DFT calculations reveal that amorphization strongly promotes the *p-d* hybridization between Co and Fe sites, significantly lowering the potential barrier of the rate-determining step that converses OH* to O* in OER [Figure 19D and E]. The structural evolution of FeCo-PO$_x$ from crystalline to amorphous can be regulated by the precursor anion etching time [Figure 19F][161]. The gained amorphous FeCo-PO$_x$ exhibits a low overpotential of 270 mV at 10 mA cm^{-2} and almost no degradation operating for 10 h, suggesting its excellent OER activity and stability [Figure 19G]. The recent reports of amorphous electrocatalyst properties in OER are concluded in Figure 19H[162-169].

ORR

The inverse reaction of OER is ORR, which is extremely important in the applications of fuel cells, metal-air batteries, sensors, and other electrochemical devices. The conversion efficiency from chemical to electrical in energy conversion devices strongly depends on ORR. Typically, there are two kinds of reaction pathways of ORR. One is reduced O$_2$ to H$_2$O or OH$^-$ via a four-electron transfer pathway in acidic and alkaline media, respectively[170]. Another pathway is reduced O$_2$ to H$_2$O$_2$ (acidic solution) or HO$_2^-$ (alkaline solution) via a two-electron transfer. Taking a four-electron transfer as an example, ORR can be expressed by the following half-reaction (Equations 17 and 18)[171].

In acidic media:

$$O_2 + 4H^+ + 4e^- \leftrightarrow 2H_2O \qquad (17)$$

In alkaline media:

$$O_2 + 2H_2O + 4e^- \leftrightarrow 4OH^- \qquad (18)$$
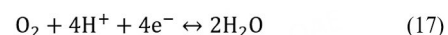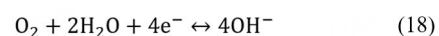
The common ORR catalysts, such as Pt-group metals and transition metal-based materials, need further optimization to realize practical applications. Amorphous ORR electrocatalysts come into being on this basis and attract marvelous concern. We summarized the recent amorphous electrocatalysts in ORR, as shown in Figure 20A[172-181]. Oxygen vacancies in amorphous catalysts play an important role in the ORR: they can provide reactive sites and act as electron transport media, participating in the electron transfer and energy level regulation on the catalyst surface, which affects the reaction rate and selectivity; at the same time, the active oxygen vacancies can react with oxygen or oxides to form intermediates of redox reactions and promote the reaction. For example, amorphous mullite SmMn$_2$O$_{5-\delta}$ nanoparticles with controllable oxygen vacancy concentration were prepared to catalyze ORR[103]. Moderate oxygen defects endow SmMn$_2$O$_{5-\delta}$ with an Mn^{3+}/Mn^{4+} ratio of 1.78 (the valence of Mn is 3.36), demonstrating excellent ORR
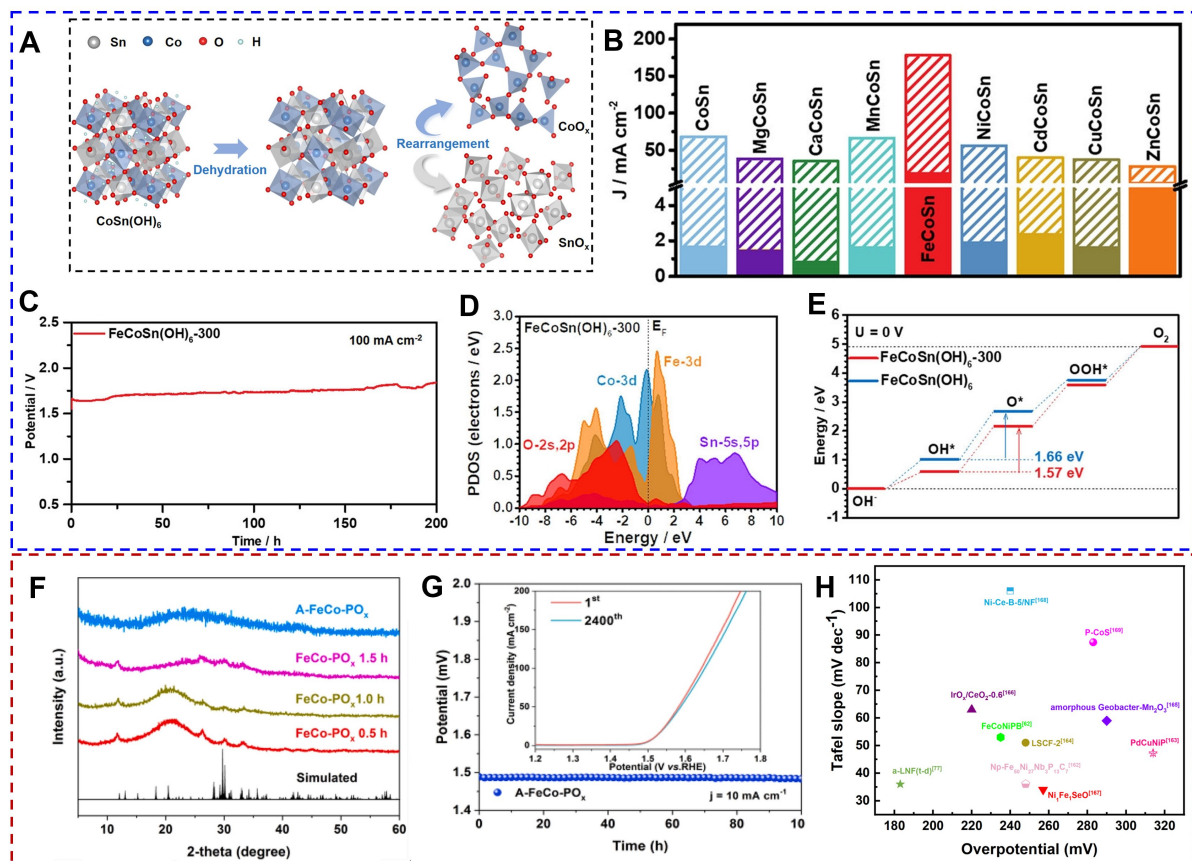
Figure 19. (A) Schematic illustration for the structural evolution of $CoSn(OH)_6$ during amorphization. (B) The current densities of $MCoSn(OH)_6$ and $MCoSn(OH)_6$-300 in O_2-saturated 1.0 M KOH solution. (C) Continuous OER chronopotentiometry test for $FeCoSn(OH)_6$-300 at 100 mA cm^{-2}. (D) The PDOS of $FeCoSn(OH)_6$-300. (E) The energetic trend of OER at U = 0 V. (Reproduced with permission[160]. Copyright 2022, Nature). (F) XRD patterns of Fe-PO_x 0.5~1.5 h and A-Fe-PO_x. (G) Chronopotentiometric curves of the long-term stability of electrodes at 10 mA cm^{-2} without iR compensation (Inset: polarization curves initial and after 2,400 CV). (Reproduced with permission[161]. Copyright 2023, Elsevier). (H) The recent reports of amorphous electrocatalyst properties in OER.

activity in alkaline solution. Their ORR performances exceed the well-crystallized $SmMn_2O_5$ (SMO) and are comparable to commercial Pt/C while reducing the undesirable product (HO_2^-) yield from 40% to less than 5%. Amorphous Fe sub-nano-clusters were grown on carbon skeletons (Fe cluster/3D-C) [Figure 20B] as ORR catalysts via a new "amino-induced spatial confinement" strategy[173]. The amorphous Fe cluster/3D-C loading small Fe (1.5 wt%) delivers a half-wave potential of 0.92 V and a mass activity of 8,600 A g_{Fe}^{-1} [Figure 20C], exceeding the benchmark commercial Pt/C (800 A g_{Pt}^{-1}). The current density maintains about 97% operating 24 h, suggesting its high durability for ORR [Figure 20D].

Amorphous Cu/Fe-NG was formed via vacuum annealing and exhibited excellent ORR activity [Figure 20E][106]. The Cu/Fe-NG features an initial potential of 1.01 V_{RHE}, a half-wave potential of 0.88 V_{RHE}, and a limiting current density of 6.01 mA cm^{-2} at 0.4 V_{RHE}, outperforming that of commercial 20 wt% Pt/C. Highly active bimetallic sites M-N_x (M = Cu, Fe) in amorphous Cu/Fe-NG were revealed via DFT calculations and contributed to enhancing its intrinsic activity [Figure 20F]. A series of amorphous manganese oxide catalysts (MnO_x-PMOD) were produced to reduce O_2. MnO_x-PMOD48 shows poor stability but superior ORR properties than that of crystalline MnO_x and MnO_x/Ti_4O_7[175]. Ti_4O_7 was further decorated on amorphous catalyst MnO_x/Ti_4O_7-PMOD to improve ORR properties. The ORR half-wave
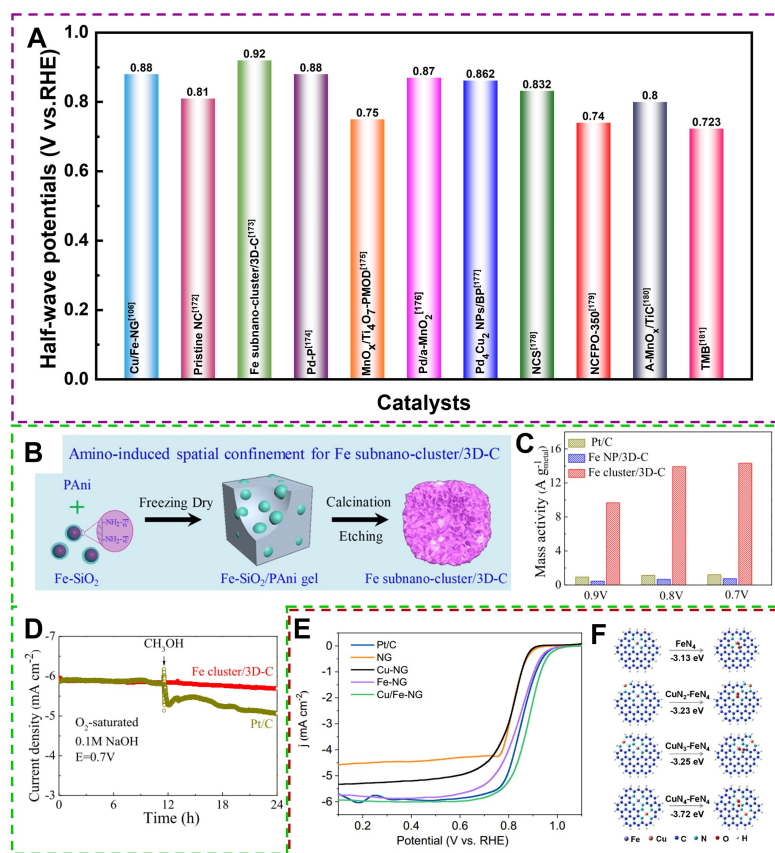
Figure 20. (A) The recent amorphous electrocatalysts in ORR. (B) Schematic of synthesis for Fe subnanocluster/3D-C. (C) Mass activity for Pt/C, Fe NP/3D-C, and Fe sub-nano-cluster/3D-C. (D) methanol tolerance tests for Fe sub-nano-cluster/3D-C. (Reproduced with permission[173]. Copyright 2019, American Chemical Society). (E) LSV curves of as-prepared catalysts and Pt/C. (F) Computational models, O_2 adsorption configurations, and corresponding adsorption energies for FeN_4 and CuN_x-FeN_4 (X = 2,3,4). (Reproduced with permission[106]. Copyright 2020, American Chemical Society).

potential of 0.75 V_{RHE} and limiting diffusion current of 5.21 mA cm^{-2} were evaluated in MnO_x/Ti_4O_7-PMOD, surpassing crystalline MnO_x/Ti_4O_7-300 catalyst. Amorphous Pd-Cr nanofibers deliver superior catalytic ORR performances in alkaline solution rather than crystalline Pd-Cr catalysts[182], such as a higher onset, positive half-wave potential, and smaller charge-transfer resistance, suggesting the excellent ORR properties of amorphous structure catalysts.

CO_2RR

CO_2RR is a transformational process designed to use renewable energy to convert greenhouse gas CO_2 into valuable carbon-based products. This reaction provides a promising way to combat climate change, develop sustainable energy, and achieve carbon-neutral energy systems. However, CO_2RR involves a variety of products, such as C_1 products (CO, HCOOH, CH_4, *etc.*), C_2 products (C_2H_4, C_2H_6, C_2H_3OH, C_2H_2OH, *etc.*), and C_{3+} products (C_3H_6, C_3H_8O, *etc.*). The reaction formulas and related theory potentials for the listed CO_2RR products can be obtained from Equations 19-27[183].

$$CO_2 + 2H^+ + 2e^- \xrightarrow{E^0_{vs.RHE}=-0.11\ V} CO + 2H_2O \tag{19}$$

$$CO_2 + 2H^+ + 2e^- \xrightarrow{E^0_{vs.RHE}=-0.12\ V} HCOOH \tag{20}$$

$$CO_2 + 8H^+ + 8e^- \xrightarrow{E^0_{vs.RHE}=0.17\ V} CH_4 + 2H_2O \tag{21}$$

$$2CO_2 + 10H^+ + 10e^- \xrightarrow{E^0_{vs.RHE}=0.06\ V} CH_3CHO + 3H_2O \tag{22}$$

$$2CO_2 + 12H^+ + 12e^- \xrightarrow{E^0_{vs.RHE}=0.08\ V} C_2H_4 + 4H_2O \tag{23}$$

$$2CO_2 + 12H^+ + 12e^- \xrightarrow{E^0_{vs.RHE}=0.09\ V} C_2H_5OH + 3H_2O \tag{24}$$

$$2CO_2 + 14H^+ + 14e^- \xrightarrow{E^0_{vs.RHE}=0.14\ V} C_2H_6 + 4H_2O \tag{25}$$

$$3CO_2 + 18H^+ + 18e^- \xrightarrow{E^0_{vs.RHE}=0.1\ V} C_3H_8O + 5H_2O \tag{26}$$

$$3CO_2 + 20H^+ + 20e^- \xrightarrow{E^0_{vs.RHE}=0.277\ V} C_3H_8 + 6H_2O \tag{27}$$
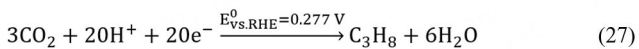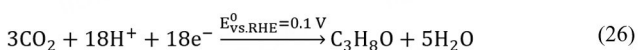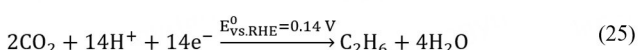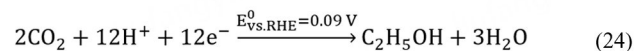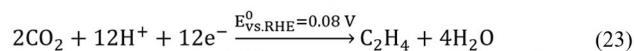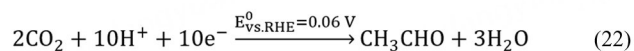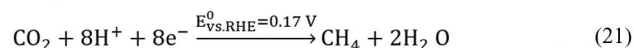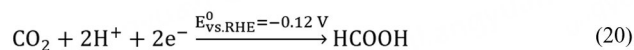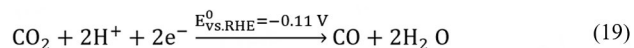
The multiple products endow CO_2RR with complex mechanisms, which can be ascribed to the formation of various reaction intermediates (*CO, *CCH, *etc.*) and different reaction pathways. Therefore, it is urgent to develop high-activity and high-selectivity electrocatalysts for CO_2RR. Amorphous CO_2RR electrocatalysts feature the merits of high activity, good selectivity, and stability, thus drawing increasing concern. We concluded the recent CO_2RR properties of amorphous electrocatalysts in Table 2.

For instance, amorphous copper nanoparticles exhibit excellent liquid product selectivity when used as CO_2RR electrocatalysts. As displayed in Figure 21A, when tested under CO_2-saturated 0.1 M $KHCO_3$ aqueous solution, the total FE based on DFT of the liquid products was up to 59% at 1.4 $V_{Ag/AgCl}$ (37% and 22% for HCOOH and C_2H_6O, respectively)[186]. The controllable amorphous copper shell can be created by supercritical CO_2 oxidation and electroreduction, and the related amorphization process is simulated in Figure 10A-F[107]. The prepared amorphous Cu shell layer in CO_2RR displays a strong selectivity for C_{2+} products [Figure 21B and C]. The FE of C_{2+} products reached 84% at -0.9 V_{RHE}, and the FE of C_{2+} oxygenates attained 65.3%, which was much greater than that of crystalline Cu. The special dendritic amorphous CuBi-100 electrocatalysts [Figure 21D] were conducted to reduce CO_2 at 0.5 M $KHCO_3$ solution and exhibited high CH_2O_2 selectivity (FE > 85%) at -0.8~-1.2 V_{RHE}[185]. The highest CH_2O_2 selectivity of 94.7% was obtained at -1.0 V_{RHE} [Figure 21E] in CuBi-100, while the highest CH_2O_2 current density of -12.8 mA cm^{-2} was measured at -1.2 V_{RHE} [Figure 21F]. The minimum R_{ct} in CuBi-100 promotes the formation of CO_2^* intermediates, thus selectively producing CH_2O_2 rather than other products.

NRR

NRR refers to the chemical process of converting N_2 into organic nitrogen compounds. The main product of NH_3 serves as a vital component in agriculture and industry. However, the thermodynamic stability of the N≡N bond and the competitive reaction of HER limit the NH_3 yield and FE. The development of high-active NRR electrocatalysts is urgent. In the developed electrocatalysts for NRR, abundant surface active sites, high surface area, porous structure, and good electron conductive endow amorphous catalysts with excellent NRR performances. We concluded the recent amorphous electrocatalysts for NRR in Table 3.

For example, amorphous $NiSb_2O_{6-x}$ nanofibers (a-$NiSb_2O_{6-x}$) with Janus structure were proposed via the different but complementary electronic structures between d- and p- block elements [Figure 22A][191]. A

Table 2. CO₂RR properties of amorphous electrocatalysts in the recent literature

Materials	Main products	Electrolytes	FE (%)	Potentials (*vs.* RHE)	Current density (mA/cm²)	Ref.
a-MnO$_x$-H	CO	0.1 M KHCO$_3$	94.8	-0.62 V	10.4	[184]
CuBi-100	Formate	0.5 M KHCO$_3$	94.7	-1.0 V	12.8	[185]
a-Cu	HCOOH	0.1 M KHCO$_3$	37	-1.4 V *vs.* Ag/AgCl	-	[186]
	C$_2$H$_6$O		22			
H-InO$_x$ NRs	HCOOH	0.5 M NaHCO$_3$	90.2	-0.8 V	7.8	[187]
P-Cd|S	CO	0.25 M K$_2$SO$_4$	88	-0.8 V	89.8	[188]
AgBi-500	HCOOH	0.1 M KHCO$_3$	94.3	-0.7 V	12.52	[189]

Table 3. NRR properties of amorphous electrocatalysts in the recent literature

Electrocatalyst	Electrolyte	NH3 yield	Potential *vs.* RHE	FE (%)	Ref.
PdCoCu NSs	0.1 M KOH	60.68 µg h^{-1}mg$_{cat}^{-1}$	-0.05 V	42.93	[190]
a-NiSb$_2$O$_{6-x}$ nanofiber	0.1 M Na$_2$SO$_4$	6.8 µg h^{-1} mg^{-1}	-0.3 V	23.3 (-0.25 V *vs.* RHE)	[191]
H-CrOx/C-550	0.1 M Na$_2$SO$_4$	19.10 µg h^{-1} mg$_{cat}^{-1}$	-0.7 V	1.4	[104]
Ni$_{0.50}$Fe$_{0.50}$B	0.1 M KOH	3.24 µg h^{-1} cm^{-2}	-0.3 V	3.19	[192]
MoS$_3$	0.5 M LiClO$_4$	51.7 µg h^{-1} mg^{-1}	-0.3 V	12.8	[193]
CoMoO$_4$	0.1 M PBS	30.2 µg h^{-1} mg$_{cat}^{-1}$	-0.5 V	3.8	[194]
BiNi	0.1M Na$_2$SO$_4$	17.5 µg h^{-1} mg$_{cat}^{-1}$	-0.6 V	13.8	[195]
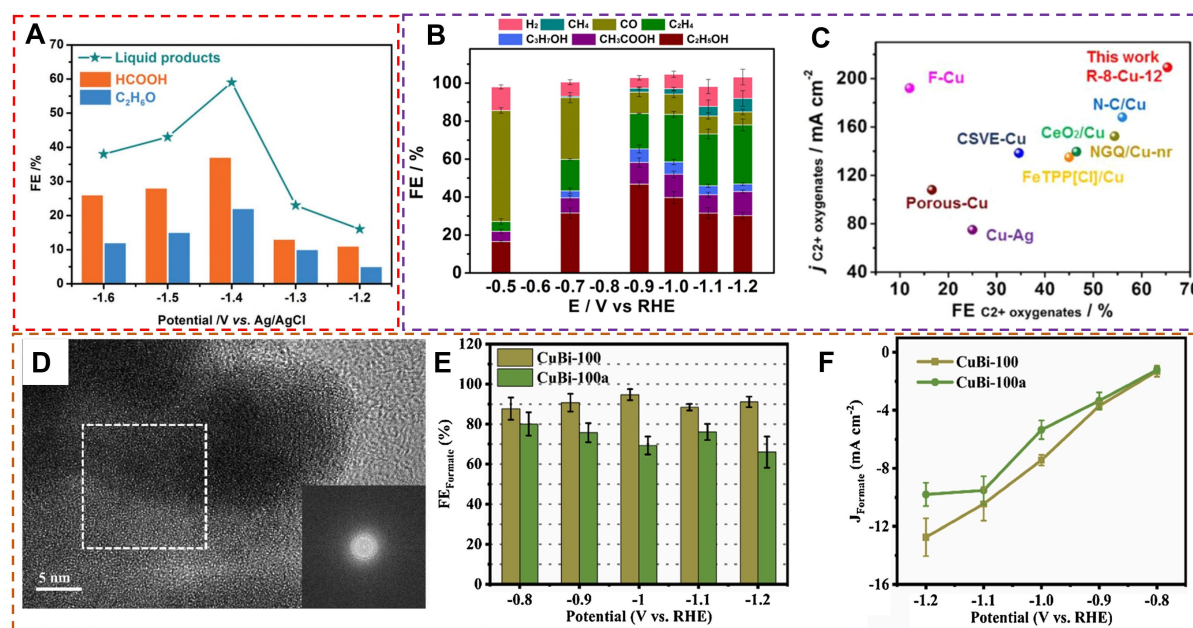
Figure 21. (A) The FE of the liquid products of a-Cu and c-Cu at each given potential for 2 h. (Reproduced with permission[186]. Copyright 2018, WILEY-VCH). (B) The distribution of C$_{2+}$ products over R-8-Cu-12. (C) The plot of C$_{2+}$ oxygenates partial current density *vs.* maximum C$_{2+}$ oxygenates FE for various catalysts. (Reproduced with permission[107]. Copyright 2023, Nature). (D) HRTEM (the inset is FFT) image of CuBi-100. (E) FE of formate for CuBi-100 and CuBi-100a. (F) Partial current density of formate for two samples in all potentials range. (Reproduced with permission[185]. Copyright 2021, Elsevier).

high NH$_3$ FE of 23.3% at -0.25 V$_{RHE}$ was obtained from a-NiSb$_2$O$_{6-x}$ [Figure 22B]. Meanwhile, the yield of NH$_3$ at -0.3 V$_{RHE}$ (6.8 µg h^{-1} mg^{-1}) is much larger than that of NiO nanofibers (2.4 µg h^{-1}mg^{-1},6.0%), Sb$_2$O$_4$
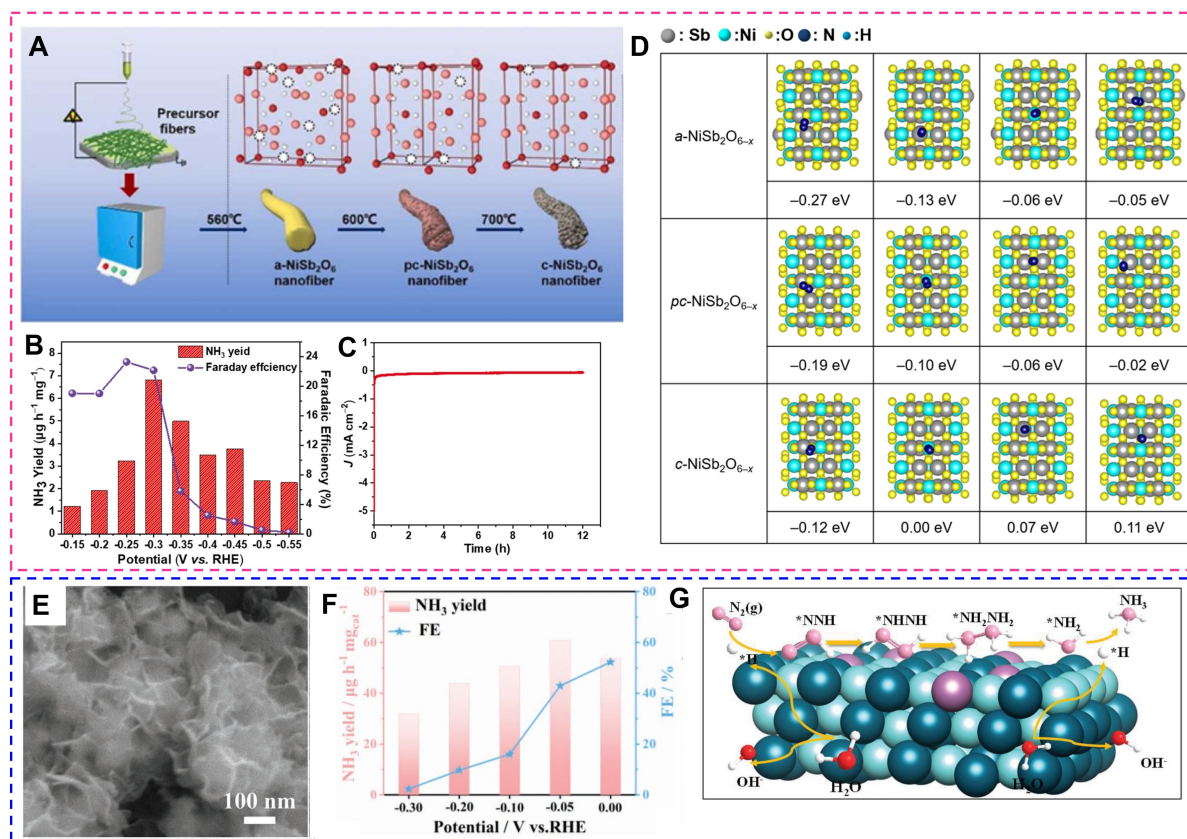
Figure 22. (A) Schematic diagram showing the process for the formation of a-$NiSb_2O_{6-x}$ nanofiber. (B) NH_3 yield and FE of a-$NiSb_2O_{6-x}$ nanofiber at each potential. (C) Chronoamperometry curve of a-$NiSb_2O_{6-x}$ nanofiber at 0.3 V_{RHE} for 12 h. (D) Binding energies of different adsorption configurations of N_2 on a-$NiSb_2O_{6-x}$, pc-$NiSb_2O_{6-x}$, and c-$NiSb_2O_{6-x}$, respectively. (Reproduced with permission[191]. Copyright 2022, Elsevier). (E) SEM image of PdCoCu NSs. (F) Histograms of average NH_3 yields and corresponding FE of PdCoCu NSs at different potentials. (G) Proposed reaction mechanism for the reduction of N_2 to NH_3. (Reproduced with permission[190]. Copyright 2023, Wiley-VCH).

nanofibers (1.5 µg h^{-1} mg^{-1}, 8.7%), and their crystal materials. Furthermore, a-$NiSb_2O_{6-x}$ nanofibers can stably operate for 12 h [Figure 22C]. Compared to the crystalline counterpart, a-$NiSb_2O_{6-x}$ exhibits a lower binding energy (-0.27 eV) and a strong adsorption capacity for N_2 by the synergy between Ni and Sb atoms [Figure 22D], thus resulting in high activity for NRR. Amorphous PdCoM (M = Cu, Ag, Fe, Mo) with 2D porous NS architectures [Figure 22E] were prepared to reduce N_2[190]. The amorphous PdCoCu delivers excellent NRR electrocatalytic activity with an NH_3 yield of 60.68 µg h^{-1} mg$_{cat}^{-1}$ and an FE of 42.93% at -0.05 V_{RHE} [Figure 22F]. Amorphous PdCoCu features a lower energy barrier for *NNH formation rather than NHNH$_2$* formation, demonstrating that the Cu atoms close to Pd atoms lower the N_2 adsorption barrier and accelerate the reaction kinetics of the crucial hydrogenation step [Figure 22G]. Moreover, MOF-base catalysts with hierarchical porous structure were prepared by Pan *et al.* for NRR[104]. In comparison to the solid and crystalline catalysts, the amorphous H-CrO$_x$/C-550 exhibits excellent NRR activity at room temperature. The NH_3 yield of amorphous H-CrO$_x$/C-550 is 19.10 µg h^{-1} mg$_{cat}^{-1}$, and the FE is 1.4% at -0.7 V_{RHE}.

SUMMARY AND PROSPECTS

This review summarized the recent advancements in classification, preparation, modification strategies, characterizations, and electrochemical applications of amorphous catalysts. Amorphous structures feature

the merits of rich chemical compositions, high specific surface area, size effect, and structural flexibility, becoming a kind of potentially efficient, stable, and controllable electrocatalysts. However, the large-scale applications of amorphous catalysts face several challenges, resulting in their further research should focus on the following aspects.

(1) Amorphous high entropy materials: Amorphous high-entropy catalysts are composed of multiple elements that form a highly disordered amorphous structure, which gives them abundant surface defects and active sites, thus enhancing their catalytic activity and selectivity. Their complex structures should be characterized by advanced characterization techniques, such as *in-situ* XPS and *in-situ* TEM, to better understand the formation and evolution of active sites in HEAs, which can lead to the design of more efficient electrocatalysts. Utilizing advantage of the adjustable composition of amorphous high-entropy catalysts and their excellent corrosion resistance and thermal stability, the catalytic performance can be precisely regulated by adjusting the composition and preparation process, which can satisfy the needs of different catalytic reactions and be applied to complex industrial catalytic environments. By taking advantage of the adjustable composition of amorphous high-entropy catalysts and their excellent corrosion resistance and thermal stability, the catalytic performance can be precisely regulated through the modulation of composition and preparation process, which can satisfy the needs of different catalytic reactions and make it applicable to complex industrial catalytic environments.

(2) Synthesis method: For the preparation methods of amorphous materials, such as rapid solidification and sputtering, which always need high temperature, high pressure, and complex processes, leading to poor controllability and high cost. Thus, developing simple and efficient methods to prepare amorphous catalysts is urgent.

(3) Large-scale preparation of amorphous materials: The development of cost-effective and scalable synthesis methods for catalysts is crucial for their practical use in industrial applications. Therefore, researchers should aim to develop efficient and controllable preparation processes that can be applied on a large scale to promote the large-scale production of amorphous catalysts. In addition, integration with advanced manufacturing technologies, such as continuous flow synthesis, microfluidics, and additive manufacturing, should be considered to improve the efficiency of amorphous catalyst production.

(4) Size effect: The high specific surface area of amorphous materials generates a microscopic size effect that extremely influences catalytic properties. Deeply revealing and precisely regulating the size effect can endow amorphous catalysts with better catalytic performances.

(5) Characterizations: The disordered feature induces the characterizations of amorphous catalysts, with remaining challenges in surface structure and active site identification. Advanced techniques of theory and experiments need to be developed to reveal the relationship between amorphous structure and catalytic activity. Meanwhile, the dynamic evolution of amorphous structures in operating urgent needs to be clarified via *in-situ* and atomic-scale characterizations, such as *in-situ* FTIR, *in-situ* XAS, *in-situ* TEM, MD, *etc*.

(6) Catalytic activity: A decisive factor for an effective catalyst, but facing the challenges of unpredictable nature and variation in amorphous catalysts. To address these issues, ML and artificial intelligence need to be developed to analyze and model large-scale experimental data. The relationship between structure and catalytic performances in amorphous catalysts can be revealed, thus guiding the design of reliable and predictable strategies for tuning catalytic activity.

(7) Coexistence of amorphous/crystalline catalyst: The coexistence of amorphous and crystalline states of catalysts may provide unique performance advantages. Amorphous structures usually have higher surface area and active sites, while crystalline structures may have better stability and conductivity. Through careful design and combining the advantages of both, more efficient catalytic performance can be achieved. Additional integration of advanced preparation techniques and materials simulation tools is pivotal in understanding the structure-property relationships of amorphous and crystalline coexisting materials. This will lead to the precise design of materials with specific structures and functions for specific catalytic reactions.

(8) Operation stability: The short-range ordered amorphous structures undergo structural changes and transform into crystalline structures during the long-term catalytic reactions, reducing catalytic activity and stability. Addressing this challenge is urgent for designing highly efficient amorphous catalysts. The usually used methods are tuning alloy compositions and surface structures; however, these approaches face several inherent issues. Therefore, novel strategies are urgently needed to develop from experimental and theoretical results, enabling amorphous catalysts to operate long-term.

(9) Catalytic mechanism: Compared with crystalline catalysts, the absence of well-defined long-range ordered structures in amorphous materials induces more complex catalytic mechanisms. Advanced characterization techniques and theoretical methods need to be developed and to reveal the catalytic mechanism of amorphous catalysts, thus guiding their rational design and optimization.

In light of the above analysis, comprehensively understanding the basic principles of amorphous catalysis and exploring new synthesis strategies are key for developing highly active and stable amorphous catalysts. Importantly, sustainability concepts need to be considered in the design and preparation of amorphous catalysts, thus minimizing environmental impact and promoting sustainable energy transition. Meanwhile, strengthening the interdisciplinary cooperation of materials science, electrochemistry, and catalysis can drive the development and applications of amorphous catalysts. We hope this review can elucidate the huge potential and current research status of amorphous structures in electrocatalysis. Moreover, this review gives a platform to understand the role, performance, and challenges of amorphous catalysts in electrocatalysis. Finally, it provides a reference for the design of high-active and stable amorphous catalysts, along with insights into their practical applications.

DECLARATIONS

Authors' contributions
Conceptualization, investigation, and writing-original draft: Yu Z, Sun Q
Writing-review & editing: Zhang M, Zhang L, Yang H, Chen Y, Guo J
Writing-review & editing, supervision, and funding acquisition: Zhang M, Zhang Z, Yu Z, Jiang Y

Availability of data and materials
Not applicable.

Financial support and sponsorship

Conflicts of interest

All authors declared that there are no conflicts of interest.

Ethical approval and consent to participate

Not applicable.

Consent for publication

Not applicable.

REFERENCES

1. Yang QR, Fan QN, Peng J, Chou SL, Liu HK, Wang J. Recent progress on alloy-based anode materials for potassium-ion batteries. *Microstructures* 2023;3:2023013. DOI
2. Yu Z, Sun Q, Li H, et al. Tuning single-phase medium-entropy oxides derived from nanoporous NiCuCoMn alloy as a highly stable anode for Li-ion batteries. *Rare Met* 2023;42:2982-92. DOI
3. Zhao SM, Wang BS, Zhu N, Huang Y, Wang F. Dual-band electrochromic materials for energy-saving smart windows. *Carbon Neutralization* 2023;2:4-27. DOI
4. Zhang Z, Xie G, Chen Y, et al. Regulating the intrinsic electronic structure of carbon nanofibers with high-spin state Ni for sodium storage with high-power density. *J Mater Sci Technol* 2024;171:16-23. DOI
5. Yan L, Zong L, Sun Q, et al. Phase separation-hydrogen etching-derived Cu-decorated Cu-Mn bimetallic oxides with oxygen vacancies boosting superior sodium-ion storage kinetics. *J Energy Chem* 2023;80:163-73. DOI
6. Chen Y, Sun H, Guo J, et al. Research on carbon-based and metal-based negative electrode materials via DFT calculation for high potassium storage performance: a review. *Energy Mater* 2023;3:300044. DOI
7. Abdelhafiz A, Wang B, Harutyunyan AR, Li J. Carbothermal shock synthesis of high entropy oxide catalysts: dynamic structural and chemical reconstruction boosting the catalytic activity and stability toward oxygen evolution reaction. *Adv Energy Mater* 2022;12:2200742. DOI
8. Li L, Dai X, Lu M, et al. Electron-enriched single-Pd-sites on g-C_3N_4 nanosheets achieved by in-situ anchoring twinned Pd nanoparticles for efficient CO_2 photoreduction. *Advanced Powder Materials* 2024;3:100170. DOI
9. Khan I, Baig N, Bake A, et al. Robust electrocatalysts decorated three-dimensional laser-induced graphene for selective alkaline OER and HER. *Carbon* 2023;213:118292. DOI
10. Li H, Du H, Luo H, Wang H, Zhu W, Zhou Y. Recent developments in metal nanocluster-based catalysts for improving photocatalytic CO_2 reduction performance. *Microstructures* 2023;3:2023024. DOI
11. Wang Y, Wang D, Li Y. Atom-level interfacial synergy of single-atom site catalysts for electrocatalysis. *J Energy Chem* 2022;65:103-15. DOI
12. Li Y, Zhang J, Chen Q, Xia X, Chen M. Emerging of heterostructure materials in energy storage: a review. *Adv Mater* 2021;33:e2100855. DOI
13. Yang Y, Li P, Zheng X, et al. Anion-exchange membrane water electrolyzers and fuel cells. *Chem Soc Rev* 2022;51:9620-93. DOI
14. Li C, Zhang Z, Chen Y, et al. Architecting braided porous carbon fibers based on high-density catalytic crystal planes to achieve highly reversible sodium-ion storage. *Adv Sci* 2022;9:e2104780. DOI PubMed PMC
15. Li H Chang SH, Zhang MM. Research progress on properties tuning and products of Cu-based catalyst in electrocatalytic CO_2 reduction. *Copper Eng* 2023;6:38-50. DOI
16. Zhang M, Wang J, Xue H, et al. Acceptor-doping accelerated charge separation in Cu_2O photocathode for photoelectrochemical water splitting: theoretical and experimental studies. *Angew Chem Int Ed* 2020;59:18463-7. DOI
17. Wang Y, Sun Y, Li H, et al. Controlled etching to immobilize highly dispersed Fe in MXene for electrochemical ammonia production. *Carbon Neutralization* 2022;1:117-25. DOI
18. Kang S, Cheng J, Gao W, Cui L. Toward safer lithium metal batteries: a review. *Energy Mater* 2023;3:300043. DOI
19. Liu H, Qin H, Kang J, et al. A freestanding nanoporous NiCoFeMoMn high-entropy alloy as an efficient electrocatalyst for rapid water splitting. *Chem Eng J* 2022;435:134898. DOI
20. Wang Z, Berbille A, Feng Y, et al. Contact-electro-catalysis for the degradation of organic pollutants using pristine dielectric powders. *Nat Commun* 2022;13:130. DOI PubMed PMC
21. Li L, Wang P, Shao Q, Huang X. Recent progress in advanced electrocatalyst design for acidic oxygen evolution reaction. *Adv Mater* 2021;33:e2004243. DOI
22. Wang Z, Richards D, Singh N. Recent discoveries in the reaction mechanism of heterogeneous electrocatalytic nitrate reduction. *Catal Sci Technol* 2021;11:705-25. DOI

23.   Ma W, He X, Wang W, Xie S, Zhang Q, Wang Y. Electrocatalytic reduction of CO_2 and CO to multi-carbon compounds over Cu-based catalysts. *Chem Soc Rev* 2021;50:12897-914. DOI

24.   Chen M, Rao P, Miao Z, et al. Strong metal-support interaction of Pt-based electrocatalysts with transition metal oxides/ nitrides/ carbides for oxygen reduction reaction. *Microstructures* 2023;3:2023025. DOI

25.   Siu JC, Fu N, Lin S. Catalyzing electrosynthesis: a homogeneous electrocatalytic approach to reaction discovery. *ACC Chem Res* 2020;53:547-60. DOI PubMed PMC

26.   Mchugh PJ, Stergiou AD, Symes MD. Decoupled electrochemical water splitting: from fundamentals to applications. *Adv Energy Mater* 2020;10:2002453. DOI

27.   Wang J, Cui W, Liu Q, Xing Z, Asiri AM, Sun X. Recent progress in cobalt-based heterogeneous catalysts for electrochemical water splitting. *Adv Mater* 2016;28:215-30. DOI

28.   Zhao C, Zhang X, Xu S, et al. Construction of amorphous $CoFeO_x(OH)_y/MoS_2/CP$ electrode for superior OER performance. *Int J Hydrogen Energy* 2022;47:28859-68. DOI

29.   Jin J, Ge J, Zhao X, Wang Y, Zhang F, Lei X. An amorphous $NiCuFeP@Cu_3P$ nanoarray for an efficient hydrogen evolution reaction. *Inorg Chem Front* 2022;9:1446-55. DOI

30.   Cheng D, Wang Z, Chen C, Zhou K. Crystalline/amorphous $Co_2P@FePO_4$ core/shell nanoheterostructures supported on porous carbon microspheres as efficient oxygen reduction electrocatalysts. *Chem Mater* 2019;31:8026-34. DOI

31.   Xu Y, Guo Y, Sheng Y, et al. Controlled boron incorporation tuned two-phase interfaces and Lewis acid sites in bismuth nanosheets for driving CO_2 electroreduction to formate. *J Mater Chem A* 2023;11:18434-40. DOI

32.   Shi M, Bao D, Li S, Wulan B, Yan J, Jiang Q. Anchoring PdCu amorphous nanocluster on graphene for electrochemical reduction of N_2 to NH_3 under ambient conditions in aqueous solution. *Adv Energy Mater* 2018;8:1800124. DOI

33.   Wang X, Tian H, Yu X, Chen L, Cui X, Shi J. Advances and insights in amorphous electrocatalyst towards water splitting. *Chin J Catal* 2023;51:5-48. DOI

34.   Zhou Y, Fan HJ. Progress and challenge of amorphous catalysts for electrochemical water splitting. *ACS Mater Lett* 2021;3:136-47. DOI

35.   Zhai W, Sakthivel T, Chen F, Du C, Yu H, Dai Z. Amorphous materials for elementary-gas-involved electrocatalysis: an overview. *Nanoscale* 2021;13:19783-811. DOI

36.   Zhang C, Wang SY, Rong JF, Mi WL. Amorphous catalysts for electrochemical water splitting. *China Pet Process Pe* 2022;24:1-13. Available from: http://www.chinarefining.com/EN/Y2022/V24/I2/1 [Last accessed on 10 Apr 2024].

37.   Wang H, Qi J, Yang N, et al. Dual-defects adjusted crystal-field splitting of $LaCo_{1-x}Ni_xO_{3-\delta}$ hollow multishelled structures for efficient oxygen evolution. *Angew Chem Int Ed* 2020;59:19691-5. DOI

38.   Anantharaj S, Noda S. Amorphous catalysts and electrochemical water splitting: an untold story of harmony. *Small* 2020;16:e1905779. DOI PubMed

39.   Dan H, Chen L, Li Z, He X, Ding Y. Preparation of amorphous ZrO_2 powders by hydrothermal-assisted sol-gel method. *Inorg Chem Commun* 2022;138:109272. DOI

40.   Liu H, Tariq NUH, Han R, et al. Development of hydrogen-free fully amorphous silicon oxycarbide coating by thermal organometallic chemical vapor deposition technique. *J Non-Cryst Solids* 2022;575:121204. DOI

41.   Wu Y, Zhang Z, Xu K, et al. A study on the formation conditions of amorphous nickel-phosphorus (Ni-P) alloy by laser-assisted electrodeposition. *Appl Surf Sci* 2021;535:147707. DOI

42.   Olowoyo JO, Kriek RJ. Recent progress on bimetallic-based spinels as electrocatalysts for the oxygen evolution reaction. *Small* 2022;18:e2203125. DOI PubMed

43.   Kumar A, Bhattacharyya S. Porous NiFe-oxide nanocubes as bifunctional electrocatalysts for efficient water-splitting. *ACS Appl Mater Interfaces* 2017;9:41906-15. DOI PubMed

44.   Nguyen TX, Liao Y, Lin C, Su Y, Ting J. Advanced high entropy perovskite oxide electrocatalyst for oxygen evolution reaction. *Adv Funct Mater* 2021;31:2101632. DOI

45.   Qiu H, Fang G, Gao J, et al. Noble metal-free nanoporous high-entropy alloys as highly efficient electrocatalysts for oxygen evolution reaction. *ACS Mater Lett* 2019;1:526-33. DOI

46.   Wang H, Liu R, Li Y, et al. Durable and efficient hollow porous oxide spinel microspheres for oxygen reduction. *Joule* 2018;2:337-48. DOI

47.   Fang L, Jiang Z, Xu H, et al. Crystal-plane engineering of $NiCo_2O_4$ electrocatalysts towards efficient overall water splitting. *J Catal* 2018;357:238-46. DOI

48.   Baek J, Hossain MD, Mukherjee P, et al. Synergistic effects of mixing and strain in high entropy spinel oxides for oxygen evolution reaction. *Nat Commun* 2023;14:5936. DOI PubMed PMC

49.   Altaf A, Sohail M, Altaf M, Nafady A, Sher M, Wahab MA. Enhanced electrocatalytic activity of amorphized $LaCoO_3$ for oxygen evolution reaction. *Chem Asian J* 2023:e202300870. DOI PubMed

50.   Smith RDL, Sporinova B, Fagan RD, Trudel S, Berlinguette CP. Facile photochemical preparation of amorphous iridium oxide films for water oxidation catalysis. *Chem Mater* 2014;26:1654-9. DOI

51.   Do VH, Prabhu P, Jose V, et al. Pd-PdO nanodomains on amorphous Ru metallene oxide for high-performance multifunctional electrocatalysis. *Adv Mater* 2023;35:e2208860. DOI

52.   Zhang L, Jang H, Liu H, et al. Sodium-decorated amorphous/crystalline RuO_2 with rich oxygen vacancies: a robust pH-universal

oxygen evolution electrocatalyst. *Angew Chem Int Ed* 2021;60:18821-9. DOI

53.   Li Y, Zhang X, Liu L, et al. Ultra-low Pt doping and Pt-Ni pair sites in amorphous/crystalline interfacial electrocatalyst enable efficient alkaline hydrogen evolution. *Small* 2023;19:e2300368. DOI

54.   Wang W, Shi X, He T, et al. Tailoring amorphous PdCu nanostructures for efficient C-C cleavage in ethanol electrooxidation. *Nano Lett* 2022;22:7028-33. DOI

55.   Jiang S, Zhu L, Yang Z, Wang Y. Self-supported hierarchical porous FeNiCo-based amorphous alloys as high-efficiency bifunctional electrocatalysts toward overall water splitting. *Int J Hydrogen Energy* 2021;46:36731-41. DOI

56.   Zhang X, Li L, Guo Y, Liu D, You T. Amorphous flower-like molybdenum-sulfide-@-nitrogen-doped-carbon-nanofiber film for use in the hydrogen-evolution reaction. *J Colloid Interface Sci* 2016;472:69-75. DOI

57.   Chen Z, Duan Z, Wang Z, et al. Amorphous cobalt oxide nanoparticles as active water-oxidation catalysts. *ChemCatChem* 2017;9:3641-5. DOI

58.   Pang Y, Xu W, Zhu S, et al. Self-supporting amorphous nanoporous NiFeCoP electrocatalyst for efficient overall water splitting. *J Mater Sci Technol* 2021;82:96-104. DOI

59.   Hu L, Zhao D, Liu C, et al. Amorphous CoB nanoarray as a high-efficiency electrocatalyst for nitrite reduction to ammonia. *Inorg Chem Front* 2022;9:6075-9. DOI

60.   Wang Z, You J, Zhao Y, et al. Research progress on high entropy alloys and high entropy derivatives as OER catalysts. *J Environ Chem Eng* 2023;11:109080. DOI

61.   Wang H, Wei R, Li X, Ma X, Hao X, Guan G. Nanostructured amorphous $Fe_{29}Co_{27}Ni_{23}Si_9B_{12}$ high-entropy-alloy: an efficient electrocatalyst for oxygen evolution reaction. *J Mater Sci Technol* 2021;68:191-8. DOI

62.   Wang Q, Li J, Li Y, Shao G, Jia Z, Shen B. Non-noble metal-based amorphous high-entropy oxides as efficient and reliable electrocatalysts for oxygen evolution reaction. *Nano Res* 2022;15:8751-9. DOI

63.   Li M, Song M, Ni W, et al. Activating surface atoms of high entropy oxides for enhancing oxygen evolution reaction. *Chin Chem Lett* 2023;34:107571. DOI

64.   Yan G, Wang Y, Zhang Z, et al. Nanoparticle-decorated ultrathin La_2O_3 nanosheets as an efficient electrocatalysis for oxygen evolution reactions. *Nanomicro Lett* 2020;12:49. DOI PubMed PMC

65.   Ghobrial S, Kirk DW, Thorpe SJ. Amorphous Ni-Nb-Y alloys as hydrogen evolution electrocatalysts. *Electrocatalysis* 2019;10:243-52. DOI

66.   Sun Y, Zhong S, Xin H, Zhang F, Chen L, Li X. Enhancement in oxidative property on amorphous rare earth doped Mn catalysts. *Catal Commun* 2016;77:94-7. DOI

67.   Gao J, Hou J, Kong L. Amorphous cobalt boride alloy synthesized by liquid phase methods as electrode materials for electrochemical capacitors. *Part Part Syst Charact* 2021;38:2100020. DOI

68.   Kong L, Dang S, Nie K, Han G, Tian G. Preparation of layered interconnected Si-Li_2MnSiO_4 electrode materials for the positive electrode of battery-type capacitors. *Ionics* 2022;28:5189-98. DOI

69.   Ye Y, Li K, Zhang W, Liu C. Precipitation of cesium lead halide perovskite nanocrystals in glasses based on liquid phase separation. *J Am Ceram Soc* 2022;105:6105-15. DOI

70.   Zhang H, Geng S, Ouyang M, Yadegari H, Xie F, Riley DJ. A self-reconstructed bifunctional electrocatalyst of pseudo-amorphous nickel carbide @ iron oxide network for seawater splitting. *Adv Sci* 2022;9:e2200146. DOI PubMed PMC

71.   Wang A, Lin B, Zhang H, et al. Ambient temperature NO oxidation over Cr-based amorphous mixed oxide catalysts: effects from the second oxide components. *Catal Sci Technol* 2017;7:2362-70. DOI

72.   Liu W, Liu H, Dang L, et al. Amorphous cobalt-iron hydroxide nanosheet electrocatalyst for efficient electrochemical and photo-electrochemical oxygen evolution. *Adv Funct Mater* 2017;27:1603904. DOI

73.   Hasannaeimi V, Wang X, Salloom R, Xia Z, Schroers J, Mukherjee S. Nanomanufacturing of non-noble amorphous alloys for electrocatalysis. *ACS Appl Energy Mater* 2020;3:12099-107. DOI

74.   Balram A, Zhang H, Santhanagopalan S. Enhanced oxygen evolution reaction electrocatalysis via electrodeposited amorphous α-phase nickel-cobalt hydroxide nanodendrite forests. *ACS Appl Mater Interfaces* 2017;9:28355-65. DOI PubMed

75.   Wang W, Zhang K, Qiao Z, Li L, Liu P, Yang Y. Hydrodeoxygenation of p-cresol on unsupported Ni-W-Mo-S catalysts prepared by one step hydrothermal method. *Catal Commun* 2014;56:17-22. DOI

76.   Esquius J, Morgan DJ, Spanos I, Hewes DG, Freakley SJ, Hutchings GJ. Effect of base on the facile hydrothermal preparation of highly active IrO_x oxygen evolution catalysts. *ACS Appl Energy Mater* 2020;3:800-9. DOI

77.   Chen G, Zhu Y, Chen HM, et al. An amorphous nickel-iron-based electrocatalyst with unusual local structures for ultrafast oxygen evolution reaction. *Adv Mater* 2019;31:e1900883. DOI

78.   Feng D, Wang P, Qin R, et al. Flower-like amorphous MoO_{3-x} stabilized Ru single atoms for efficient overall water/seawater splitting. *Adv Sci* 2023;10:e2300342. DOI PubMed PMC

79.   Zhong R, Liao Y, Peng L, et al. Silica-carbon nanocomposite acid catalyst with large mesopore interconnectivity by vapor-phase assisted hydrothermal treatment. *ACS Sustain Chem Eng* 2018;6:7859-70. DOI

80.   Karki S, Ingole PG. Development of polymer-based new high performance thin-film nanocomposite nanofiltration membranes by vapor phase interfacial polymerization for the removal of heavy metal ions. *Chem Eng J* 2022;446:137303. DOI

81.   Xia J, Li XZ, Huang X, et al. Physical vapor deposition synthesis of two-dimensional orthorhombic SnS flakes with strong angle/temperature-dependent Raman responses. *Nanoscale* 2016;8:2063-70. DOI

82. Grüner C, Liedtke S, Bauer J, Mayr SG, Rauschenbach B. Morphology of thin films formed by oblique physical vapor deposition. *ACS Appl Nano Mater* 2018;1:1370-6. DOI

83. Wei TR, Zhang SS, Liu Q, Qiu Y, Luo J, Liu X. Oxygen vacancy-rich amorphous copper oxide enables highly selective electroreduction of carbon dioxide to ethylene. *Acta Physico Chimica Sinica* 2022;2:20220702. DOI

84. Hong YL, Liu Z, Wang L, et al. Chemical vapor deposition of layered two-dimensional $MoSi_2N_4$ materials. *Science* 2020;369:670-4. DOI

85. Zhang ZJ, Sun HY, Chen YF, et al. Modulating p-d orbital hybridization by CuO/Cu nanoparticles enables carbon nanofibers high cycling stability as anode for sodium storage. *Rare Met* 2023;42:4039-47. DOI

86. Su G, Hadjiev VG, Loya PE, et al. Chemical vapor deposition of thin crystals of layered semiconductor SnS_2 for fast photodetection application. *Nano Lett* 2015;15:506-13. DOI

87. Wu G, Zheng X, Cui P, et al. A general synthesis approach for amorphous noble metal nanosheets. *Nat Commun* 2019;10:4855. DOI PubMed PMC

88. Li K, Chen W. Recent progress in high-entropy alloys for catalysts: synthesis, applications, and prospects. *Mater Today Energy* 2021;20:100638. DOI

89. Ricciardella F, Vollebregt S, Kurganova E, Giesbers AJM, Ahmadi M, Sarro PM. Growth of multi-layered graphene on molybdenum catalyst by solid phase reaction with amorphous carbon. *2D Mater* 2019;6:035012. DOI

90. Sundeev R, Shalimova A, Veligzhanin A, Glezer A, Zubavichus Y. Difference between local atomic structures of the amorphous Ti_2NiCu alloy prepared by melt quenching and severe plastic deformation. *Mater Lett* 2018;214:115-8. DOI

91. Yang X, Xu W, Cao S, et al. An amorphous nanoporous PdCuNi-S hybrid electrocatalyst for highly efficient hydrogen production. *Appl Catal B Environ* 2019;246:156-65. DOI

92. Li H, Zhu Z, Wang Y, Chen S, Liu C, Zhang H. Disordered and oxygen vacancy-rich NiFe hydroxides/oxides in situ grown on amorphous ribbons for boosted alkaline water oxidation. *J Electroanal Chem* 2021;880:114918. DOI

93. Wang ZJ, Li MX, Yu JH, Ge XB, Liu YH, Wang WH. Low-iridium-content IrNiTa metallic glass films as intrinsically active catalysts for hydrogen evolution reaction. *Adv Mater* 2020;32:e1906384. DOI PubMed

94. Gou J, Qiao Z, Yu Z, et al. Architecting a 3D continuous $C/CuVO_3@Cu$ composite anode for lithium-ion storage. *Surf Innov* 2023;11:70-8. DOI

95. Cole KM, Prabhudev S, Botton GA, Kirk DW, Thorpe SJ. Amorphous Ni-based nanoparticles for alkaline oxygen evolution. *ACS Appl Nano Mater* 2020;3:10522-30. DOI

96. Duan Y, Yu ZY, Hu SJ, et al. Scaled-up synthesis of amorphous NiFeMo oxides and their rapid surface reconstruction for superior oxygen evolution catalysis. *Angew Chem Int Ed* 2019;58:15772-7. DOI

97. Li Z, Xie Y, Huang Z, et al. Amorphization of $LaCoO_3$ perovskite nanostructures for efficient oxygen evolution. *ACS Appl Nano Mater* 2022;5:14209-15. DOI

98. Zhang M, Xu W, Ma CL, Yu J, Liu YT, Ding B. Highly active and selective electroreduction of N_2 by the catalysis of Ga single atoms stabilized on amorphous TiO_2 nanofibers. *ACS Nano* 2022;16:4186-96. DOI

99. Lu J, Chen S, Zhuo Y, Mao X, Liu D, Wang Z. Greatly boosting seawater hydrogen evolution by surface amorphization and morphology engineering on $MoO_2/Ni_3(PO_4)_2$. *Adv Funct Mater* 2023;33:2308191. DOI

100. Li X, Cai W, Li D, Xu J, Tao H, Liu B. Amorphous alloys for electrocatalysis: the significant role of the amorphous alloy structure. *Nano Res* 2023;16:4277-88. DOI

101. Shen Y, Mai Y. Structural studies of amorphous and crystallized tungsten nitride thin films by EFED, XRD and TEM. *Appl Surf Sci* 2000;167:59-68. DOI

102. Zhan C, Huang D, Hu X, et al. Mechanical property enhancement of NbTiZr refractory medium-entropy alloys due to Si-induced crystalline-to-amorphous transitions. *Surf Coat Technol* 2022;433:128144. DOI

103. Dong C, Liu ZW, Liu JY, et al. Modest oxygen-defective amorphous manganese-based nanoparticle mullite with superior overall electrocatalytic performance for oxygen reduction reaction. *Small* 2017;13:1603903. DOI

104. Pan T, Wang L, Shen Y, et al. Amorphous chromium oxide with hollow morphology for nitrogen electrochemical reduction under ambient conditions. *ACS Appl Mater Interfaces* 2022;14:14474-81. DOI

105. Meng X, Yuan B, Liu Y, Zhao Z, Li K, Lin Y. Amorphous Fe-Mo-O nanostructures for catalytic water oxidation. *ACS Appl Nano Mater* 2022;5:9427-34. DOI

106. Xu L, Tian Y, Deng D, et al. Cu nanoclusters/FeN_4 amorphous composites with dual active sites in n-doped graphene for high-performance Zn-Air batteries. *ACS Appl Mater Interfaces* 2020;12:31340-50. DOI

107. Chen C, Yan X, Wu Y, et al. Oxidation of metallic Cu by supercritical CO_2 and control synthesis of amorphous nano-metal catalysts for CO_2 electroreduction. *Nat Commun* 2023;14:1092. DOI PubMed PMC

108. Kang J, Yang X, Hu Q, Cai Z, Liu LM, Guo L. Recent progress of amorphous nanomaterials. *Chem Rev* 2023;123:8859-941. DOI

109. Banko L, Krysiak OA, Pedersen JK, et al. Unravelling composition-activity-stability trends in high entropy alloy electrocatalysts by using a data-guided combinatorial synthesis strategy and computational modeling. *Adv Energy Mater* 2022;12:2103312. DOI

110. Huang J, Fu C, Chen J, Senthilkumar N, Peng X, Wen Z. The enhancement of selectivity and activity for two-electron oxygen reduction reaction by tuned oxygen defects on amorphous hydroxide catalysts. *CCS Chem* 2022;4:566-83. DOI

111. Fang Z, Shen B, Lu J, Fan K, Deng J. DFT study of electron transfer between B and Ni in Ni-B amorphous alloy. *Acta Chimica Sinica* 1999;57:894-900. Available from: https://sioc-journal.cn/Jwk_hxxb/EN/Y1999/V57/I8/894 [Last accessed on 9 Apr 2024].

112. He Y, Liu L, Zhu C, et al. Amorphizing noble metal chalcogenide catalysts at the single-layer limit towards hydrogen production. *Nat Catal* 2022;5:212-21. DOI

113. Zhang D, Li H, Lu H, et al. Unlocking the performance of ternary metal (hydro)oxide amorphous catalysts *via* data-driven active-site engineering. *Energy Environ Sci* 2023;16:5065-75. DOI

114. Bui TS, Lovell EC, Daiyan R, Amal R. Defective metal oxides: lessons from CO_2 RR and applications in NO_xRR. *Adv Mater* 2023;35:e2205814. DOI

115. Ye L, Wang J, Zhang Y, Zhang M, Jing X, Gong Y. A self-supporting electrode with in-situ partial transformation of Fe-MOF into amorphous NiFe-LDH for efficient oxygen evolution reaction. *Appl Surf Sci* 2021;556:149781. DOI

116. Zhao J, Ren X, Ma H, et al. Synthesis of self-supported amorphous $CoMoO_4$ nanowire array for highly efficient hydrogen evolution reaction. *ACS Sustain Chem Eng* 2017;5:10093-8. DOI

117. Yang P, Wang B, Liu Z. Towards activation of amorphous MoS_x via Cobalt doping for enhanced electrocatalytic hydrogen evolution reaction. *Int J Hydrogen Energy* 2018;43:23109-17. DOI

118. Wang D, Xie Y, Wu Z. Amorphous phosphorus-doped MoS_2 catalyst for efficient hydrogen evolution reaction. *Nanotechnology* 2019;30:205401. DOI

119. Ren H, Sun X, Du C, et al. Amorphous Fe-Ni-P-B-O nanocages as efficient electrocatalysts for oxygen evolution reaction. *ACS Nano* 2019;13:12969-79. DOI

120. Dhandapani H, Madhu R, De A, Salem MA, Ramesh Babu B, Kundu S. Tuning the surface electronic structure of amorphous $NiWO_4$ by doping Fe as an electrocatalyst for OER. *Inorg Chem* 2023;62:11817-28. DOI PubMed

121. Sun J, Guo N, Shao Z, et al. A facile strategy to construct amorphous spinel-based electrocatalysts with massive oxygen vacancies using ionic liquid dopant. *Adv Energy Mater* 2018;8:1800980. DOI

122. Gao YQ, Liu XY, Yang GW. Amorphous mixed-metal hydroxide nanostructures for advanced water oxidation catalysts. *Nanoscale* 2016;8:5015-23. DOI PubMed

123. Yang M, Zhao M, Yuan J, et al. Oxygen vacancies and interface engineering on amorphous/crystalline CrO_x-Ni_3 N heterostructures toward high-durability and kinetically accelerated water splitting. *Small* 2022;18:e2106554. DOI

124. Gao L, Guo C, Sun X, et al. $CoFeO_x(OH)_y$/$CoO_x(OH)_y$ core/shell structure with amorphous interface as an advanced catalyst for electrocatalytic water splitting. *Electrochim Acta* 2020;341:136038. DOI

125. Sun A, Qiu Y, Wang Z, et al. Interface engineering on super-hydrophilic amorphous/crystalline NiFe-based hydroxide/selenide heterostructure nanoflowers for accelerated industrial overall water splitting at high current density. *J Colloid Interface Sci* 2023;650:573-81. DOI

126. Zhang HM, Zuo LH, Gao YH, et al. Amorphous high-entropy phosphoxides for efficient overall alkaline water/seawater splitting. *J Mater Sci Technol* 2023;173:1-10. DOI

127. Cheng C, Liu T, Wang Y, et al. Amorphous $Sn(HPO_4)_2$-derived phosphorus-modified Sn/SnO core/shell catalyst for efficient CO_2 electroreduction to formate. *J Energy Chem* 2023;81:125-31. DOI

128. Smith G, Brower W, Matyjaszczyk M, Pettit T. Metallic glasses: new catalyst systems. *Stud Surf Sci Catal* 1981;7:355-63. DOI

129. Kreysa G, Håkansson B. Electrocatalysis by amorphous metals of hydrogen and oxygen evolution in alkaline solution. *J Electroanal Chem Interfacial Electrochem* 1986;201:61-83. DOI

130. Lian K, Thorpe S, Kirk D. Electrochemical and surface characterization of electrocatalytically active amorphous Ni Co alloys. *Electrochim Acta* 1992;37:2029-41. DOI

131. Deng J, Li H, Wang W. Progress in design of new amorphous alloy catalysts. *Catal Today* 1999;51:113-25. DOI

132. Janik-czachor M, Szummer A, Molnar A, et al. Electrochemical modification of Cu-Zr amorphous alloys for catalysts. *Electrochim Acta* 2000;45:3295-304. DOI

133. Li H, Xu Y. Liquid phase benzene hydrogenation to cyclohexane over modified Ni-P amorphous catalysts. *Mater Lett* 2001;51:101-7. DOI

134. Ramos-sánchez G, Pierna A, Solorza-feria O. Amorphous $Ni_{59}Nb_{40}Pt_xM_{1-x}$ (M=Ru,Sn) electrocatalysts for oxygen reduction reaction. *J Non-Cryst Solids* 2008;354:5165-8. DOI

135. Fernandes R, Patel N, Miotello A. Efficient catalytic properties of Co-Ni-P-B catalyst powders for hydrogen generation by hydrolysis of alkaline solution of $NaBH_4$. *Int J Hydrogen Energy* 2009;34:2893-900. DOI

136. Fugane K, Mori T, Ou DR, et al. Activity of oxygen reduction reaction on small amount of amorphous CeO_x promoted Pt cathode for fuel cell application. *Electrochim Acta* 2011;56:3874-83. DOI

137. Cavalca F, Ferragut R, Aghion S, et al. Nature and distribution of stable subsurface oxygen in copper electrodes during electrochemical CO_2 reduction. *J Phys Chem C* 2017;121:25003-9. DOI

138. Lv CD, Yan CS, Chen G, et al. An amorphous noble-metal-free electrocatalyst that enables nitrogen fixation under ambient conditions. *Angew Chem Int Ed* 2018;130:6181-6184. DOI

139. Tielens F, Gierada M, Handzlik J, Calatayud M. Characterization of amorphous silica based catalysts using DFT computational methods. *Catal Today* 2020;354:3-18. DOI

140. Liu H, Xi C, Xin J, et al. Free-standing nanoporous NiMnFeMo alloy: an efficient non-precious metal electrocatalyst for water splitting. *Chem Eng J* 2021;404:126530. DOI

141. Pu Z, Amiinu IS, Cheng R, et al. Single-atom catalysts for electrochemical hydrogen evolution reaction: recent advances and future

perspectives. *Nanomicro Lett* 2020;12:21.　DOI　PubMed　PMC

142.　Zheng X, Li P, Dou S, et al. Non-carbon-supported single-atom site catalysts for electrocatalysis. *Energy Environ Sci* 2021;14:2809-58.　DOI

143.　Al-naggar AH, Shinde NM, Kim J, Mane RS. Water splitting performance of metal and non-metal-doped transition metal oxide electrocatalysts. *Coord Chem Rev* 2023;474:214864.　DOI

144.　Xing M, Zhu S, Zeng X, Wang S, Liu Z, Cao D. Amorphous/Crystalline Rh(OH)$_3$/CoP heterostructure with hydrophilicity/ aerophobicity feature for all-pH hydrogen evolution reactions. *Adv Energy Mater* 2023;13:2302376.　DOI

145.　Cao D, Dong Y, Tang Y, et al. Amorphous manganese-cobalt nanosheets as efficient catalysts for hydrogen evolution reaction (HER). *Catal Surv Asia* 2021;25:437-44.　DOI

146.　Xia Y, Wu W, Wang H, Rao S, Zhang F, Zou G. Amorphous RuS$_2$ electrocatalyst with optimized active sites for hydrogen evolution. *Nanotechnology* 2020;31:145401.　DOI　PubMed

147.　Zhang X, Li K, Wen B, Ma J, Diao D. Machine learning accelerated DFT research on platinum-modified amorphous alloy surface catalysts. *Chin Chem Lett* 2023;34:107833.　DOI

148.　Zhang J, Wu Y, Hao H, et al. Construction of amorphous Fe$_{0.95}$S$_{1.05}$ nanorods with high electrocatalytic activity for enhanced hydrogen evolution reaction. *Electrochim Acta* 2022;402:139554.　DOI

149.　Wu G, Han X, Cai J, et al. In-plane strain engineering in ultrathin noble metal nanosheets boosts the intrinsic electrocatalytic hydrogen evolution activity. *Nat Commun* 2022;13:4200.　DOI　PubMed　PMC

150.　Chunduri A, Bhide A, Gupta S, et al. Exploring the role of multi-catalytic sites in an amorphous Co-W-B electrocatalyst for hydrogen and oxygen evolution reactions. *ACS Appl Energy Mater* 2023;6:4630-41.　DOI

151.　Shao G, Wang Q, Miao F, Li J, Li Y, Shen B. Improved catalytic efficiency and stability by surface activation in Fe-based amorphous alloys for hydrogen evolution reaction in acidic electrolyte. *Electrochim Acta* 2021;390:138815.　DOI

152.　Yu J, Li A, Li L, Li X, Wang X, Guo L. Morphological and structural engineering in amorphous Cu$_2$MoS$_4$ nanocages for remarkable electrocatalytic hydrogen evolution. *Sci China Mater* 2019;62:1275-84.　DOI

153.　Zhao L, Chang B, Dong T, et al. Laser synthesis of amorphous CoS$_x$ nanospheres for efficient hydrogen evolution and nitrogen reduction reactions. *J Mater Chem A* 2022;10:20071-9.　DOI

154.　Lu W, Li X, Wei F, et al. In-situ transformed Ni, S-Codoped CoO from amorphous Co-Ni sulfide as an efficient electrocatalyst for hydrogen evolution in alkaline media. *ACS Sustain Chem Eng* 2019;7:12501-9.　DOI

155.　Hu M, Qian Y, Yu S, et al. Amorphous MoS$_2$ decorated Ni$_3$S$_2$ with a core-shell structure of urchin-like on nickel-foam efficient hydrogen evolution in acidic and alkaline media. *Small* 2024;20:e2305948.　DOI

156.　Ge Y, Ge J, Huang B, et al. Synthesis of amorphous Pd-based nanocatalysts for efficient alcoholysis of styrene oxide and electrochemical hydrogen evolution. *Nano Res* 2023;16:4650-5.　DOI

157.　Bodhankar PM, Sarawade PB, Kumar P, et al. Nanostructured metal phosphide based catalysts for electrochemical water splitting: a review. *Small* 2022;18:e2107572.　DOI

158.　Jamesh M, Sun X. Recent progress on earth abundant electrocatalysts for oxygen evolution reaction (OER) in alkaline medium to achieve efficient water splitting - a review. *J Power Sources* 2018;400:31-68.　DOI

159.　Li X, Zhang H, Hu Q, et al. Amorphous NiFe oxide-based nanoreactors for efficient electrocatalytic water oxidation. *Angew Chem Int Ed* 2023;62:e202300478.　DOI

160.　Liu S, Geng S, Li L, et al. A top-down strategy for amorphization of hydroxyl compounds for electrocatalytic oxygen evolution. *Nat Commun* 2022;13:1187.　DOI　PubMed　PMC

161.　Liu X, Yin H, Zhang S, et al. Revealing the effect of crystallinity and oxygen vacancies of Fe-Co phosphate on oxygen evolution for high-current water splitting. *J Colloid Interface Sci* 2024;653:1379-87.　DOI

162.　Xiao L, Liang Y, Li Z, et al. Amorphous FeNiNbPC nanoprous structure for efficient and stable electrochemical oxygen evolution. *J Colloid Interface Sci* 2022;608:1973-82.　DOI

163.　Zheng Y, Guo R, Li X, et al. Synthesis of amorphous trimetallic PdCuNiP nanoparticles for enhanced OER. *Front Chem* 2023;11:1122333.　DOI　PubMed　PMC

164.　Zhao C, Li N, Zhang R, et al. Surface reconstruction of La$_{0.8}$Sr$_{0.2}$Co$_{0.8}$Fe$_{0.2}$O$_{3-\delta}$ for superimposed OER performance. *ACS Appl Mater Interfaces* 2019;11:47858-67.　DOI

165.　Kalathil S, Katuri KP, Saikaly PE. Synthesis of an amorphous *Geobacter* -manganese oxide biohybrid as an efficient water oxidation catalyst. *Green Chem* 2020;22:5610-8.　DOI

166.　Gou W, Xia Z, Tan X, et al. Highly active and stable amorphous IrO$_x$/CeO$_2$ nanowires for acidic oxygen evolution. *Nano Energy* 2022;104:107960.　DOI

167.　Zhang L, Lu C, Ye F, et al. Vacancies boosting strategy enabling enhanced oxygen evolution activity in a library of novel amorphous selenite electrocatalysts. *Appl Catal B Environ* 2021;284:119758.　DOI

168.　Wang S, Zhao R, Zheng T, et al. Cerium decorated amorphous ternary Ni-Ce-B catalyst for enhanced electrocatalytic water oxidation. *Surf Interfaces* 2021;26:101447.　DOI

169.　Li Z, Li C, Huang J, et al. Structure engineering of amorphous P-CoS hollow electrocatalysts for promoted oxygen evolution reaction. *Int J Hydrogen Energy* 2022;47:15189-97.　DOI

170.　Kim C, Dionigi F, Beermann V, Wang X, Möller T, Strasser P. Alloy nanocatalysts for the electrochemical oxygen reduction (ORR) and the direct electrochemical carbon dioxide reduction reaction (CO$_2$RR). *Adv Mater* 2019;31:e1805617.　DOI　PubMed

171. Tian J, Shen Y, Liu P, et al. Recent advances of amorphous-phase-engineered metal-based catalysts for boosted electrocatalysis. *J Mater Sci Technol* 2022;127:1-18. DOI

172. Biemolt J, Rothenberg G, Yan N. Understanding the roles of amorphous domains and oxygen-containing groups of nitrogen-doped carbon in oxygen reduction catalysis: toward superior activity. *Inorg Chem Front* 2020;7:177-85. DOI

173. Liu L, Zhao X, Li R, Su H, Zhang H, Liu Q. Subnano amorphous Fe-based clusters with high mass activity for efficient electrocatalytic oxygen reduction reaction. *ACS Appl Mater Interfaces* 2019;11:41432-9. DOI

174. Poon KC, Tan DC, Vo TD, et al. Newly developed stepwise electroless deposition enables a remarkably facile synthesis of highly active and stable amorphous Pd nanoparticle electrocatalysts for oxygen reduction reaction. *J Am Chem Soc* 2014;136:5217-20. DOI

175. Bai F, He Y, Xu L, et al. Improved ORR/OER bifunctional catalytic performance of amorphous manganese oxides prepared by photochemical metal-organic deposition. *RSC Adv* 2022;12:2408-15. DOI PubMed PMC

176. Wang Y, Liu J, Yuan H, Liu F, Hu T, Yang B. Strong electronic interaction between amorphous MnO_2 nanosheets and ultrafine Pd nanoparticles toward enhanced oxygen reduction and ethylene glycol oxidation reactions. *Adv Funct Mater* 2023;33:2211909. DOI

177. Li W, Fu W, Bai S, et al. Inspired electrocatalytic performance by unique amorphous PdCu nanoparticles on black phosphorus. *Electrochim Acta* 2023;446:142082. DOI

178. Li Q, Kong D, Zhao X, et al. Short-range amorphous carbon nanosheets for oxygen reduction electrocatalysis. *Nanoscale Adv* 2020;2:5769-76. DOI PubMed PMC

179. Pan D, Chen P, Zhou L, Liu J, Guo Z, Song J. Self-template construction of 2D amorphous N-doped CoFe-mesoporous phosphate microsheets for zinc-air batteries. *J Power Sources* 2021;498:229859. DOI

180. Song S, Li W, Deng Y, et al. TiC supported amorphous MnOx as highly efficient bifunctional electrocatalyst for corrosion resistant oxygen electrode of Zn-air batteries. *Nano Energy* 2020;67:104208. DOI

181. Moloudi M, Noori A, Rahmanifar MS, et al. Layered double hydroxide templated synthesis of amorphous NiCoFeB as a multifunctional electrocatalyst for overall water splitting and rechargeable zinc-air batteries. *Adv Energy Mater* 2023;13:2203002. DOI

182. Jin D, Lee Y, Kim IY, Lee C, Kim MH. Impact of controlling the crystallinity on bifunctional electrocatalytic performances toward methanol oxidation and oxygen reduction in binary Pd-Cr solid solution. *J Mater Chem A* 2023;11:16243-54. DOI

183. Yao Y, Zhuang W, Li R, et al. Sn-based electrocatalysts for electrochemical CO_2 reduction. *Chem Commun* 2023;59:9017-28. DOI

184. Han H, Jin S, Park S, et al. Plasma-induced oxygen vacancies in amorphous MnOx boost catalytic performance for electrochemical CO_2 reduction. *Nano Energy* 2021;79:105492. DOI

185. Xiong Y, Wei B, Wu M, et al. Rapid synthesis of amorphous bimetallic copper-bismuth electrocatalysts for efficient electrochemical CO_2 reduction to formate in a wide potential window. *J CO₂ Util* 2021;51:101621. DOI

186. Duan YX, Meng FL, Liu KH, et al. Amorphizing of Cu nanoparticles toward highly efficient and robust electrocatalyst for CO_2 reduction to liquid fuels with high faradaic efficiencies. *Adv Mater* 2018;30:e1706194. DOI

187. Zhang J, Yin R, Shao Q, Zhu T, Huang X. Oxygen vacancies in amorphous InO_x nanoribbons enhance CO_2 adsorption and activation for CO_2 electroreduction. *Angew Chem Int Ed* 2019;58:5609-13. DOI

188. Wu Y, Zhai P, Cao S, et al. Beyond d orbits: steering the selectivity of electrochemical CO_2 reduction via hybridized sp band of sulfur-incorporated porous Cd architectures with dual collaborative sites. *Adv Energy Mater* 2020;10:2002499. DOI

189. Zhou JH, Yuan K, Zhou L, et al. Boosting electrochemical reduction of CO_2 at a low overpotential by amorphous Ag-Bi-S-O decorated Bi_0 nanocrystals. *Angew Chem Int Ed* 2019;58:14197-201. DOI

190. Dong Z, Sun Q, Xu GR, et al. Universal synthesized strategy for amorphous Pd-Based nanosheets boosting ambient ammonia electrosynthesis. *Small Methods* 2023;7:e2201225. DOI

191. Xu W, Zhang M, Ma C, Wu S, Liu Y. Amorphous $NiSb_2O_{6-x}$ nanofiber: a d-/p-block Janus electrocatalyst toward efficient NH_3 synthesis through boosted N_2 adsorption and activation. *Appl Catal B Environ* 2022;308:121225. DOI

192. Wang Y, Tian Y, Zhang J, et al. Tuning morphology and electronic structure of amorphous NiFeB nanosheets for enhanced electrocatalytic N_2 reduction. *ACS Appl Energy Mater* 2020;3:9516-22. DOI

193. Chu K, Nan H, Li Q, Guo Y, Tian Y, Liu W. Amorphous MoS_3 enriched with sulfur vacancies for efficient electrocatalytic nitrogen reduction. *J Energy Chem* 2021;53:132-8. DOI

194. Xiao L, Liang Y, Li Z, et al. Amorphous $CoMoO_4$ with nanoporous structures for electrochemical ammonia synthesis under ambient conditions. *ACS Sustain Chem Eng* 2020;8:19072-83. DOI

195. Fang Z, Wu P, Qian Y, Yu G. Gel-derived amorphous bismuth-nickel alloy promotes electrocatalytic nitrogen fixation via optimizing nitrogen adsorption and activation. *Angew Chem Int Ed* 2021;60:4275-81. DOI PubMed